AGU PUBLICATIONS

JGR

Journal of Geophysical Research: Oceans

RESEARCH ARTICLE

10.1002/2014JC010541

Observed and modeled drifters at a tidal inlet

Matthew S. Spydell[1], Falk Feddersen[1], Maitane Olabarrieta[2], Jialin Chen[3], R. T. Guza[1], Britt Raubenheimer[4], and Steve Elgar[4]

[1]Integrative Oceanography Division, Scripps Institution of Oceanography, La Jolla, California, USA, [2]Department of Civil and Coastal Engineering, University of Florida, Gainesville, Florida, USA, [3]Civil and Environmental Engineering, University of Delaware, Newark, Delaware, USA, [4]Woods Hole Oceanographic Institution, Woods Hole, Massachusetts, USA

Key Points:
- Observed drifter and current meter velocities are similar within a tidal inlet
- Observed drifter spreading is larger than modeled during ebb tide
- Observed spreading rates are likely affected by stratification

Correspondence to:
M. S. Spydell,
mspydell@ucsd.edu

Citation:
Spydell, M. S., F. Feddersen, M. Olabarrieta, J. Chen, R. T. Guza, B. Raubenheimer, and S. Elgar (2015), Observed and modeled drifters at a tidal inlet, *J. Geophys. Res. Oceans*, *120*, doi:10.1002/2014JC010541.

Received 28 OCT 2014
Accepted 9 JUN 2015
Accepted article online 12 JUN 2015

Abstract Material transport and dispersion near the mouth of a tidal inlet (New River Inlet, NC) are investigated using GPS-tracked drifters and numerical models. For ebb tide releases, velocities are largest (>1 m s^{-1}) in two approximately 30 m wide channels that bisect the 1–3 m deep ebb shoal. In the channels, drifter and subsurface current meter velocities are similar, consistent with strong vertical mixing and 2-D hydrodynamics. Drifters were preferentially entrained in the channelized jets where drifter cluster lateral spreading rates μ_{in} were small ($\mu_{in} \approx 0.5$ m^2 s^{-1}). At the seaward edge of the ebb shoal, jet velocities decrease linearly with distance (to ≤ 0.2 m s^{-1}, about 1 km from shore), and cluster spreading rates are larger with $\mu_{out} \approx 3$ m^2 s^{-1}. Although the models COAWST and NearCom generally reproduce the observed trajectory directions, certain observed drifter properties are poorly modeled. For example, modeled mean drifter velocities are smaller than observed, and upon exiting the inlet, observed drifters turn north more than modeled drifters. The model simulations do reproduce qualitatively the spreading rates observed in the inner inlet, the flow deceleration, and the increase in μ_{out} observed in the outer inlet. However, model spreading rates increase only to $\mu_{out} < 1$ m^2 s^{-1}. Smaller modeled than observed μ_{out} may result from using unstratified models. Noncoincident (in space) observations show evidence of a buoyant plume ($\Delta\rho = 1$ kg m^{-3}) in the outer inlet, likely affecting drifter lateral spreading. Generally, drifter-based model performance is good within the inlet channels where tidal currents are strongest, whereas model-data differences are significant farther offshore.

1. Introduction

Tidal inlets are important transitional regions between estuaries, bays, lagoons, marshes, and the coastal ocean, and are ubiquitous features of barrier island geography. Tidal inlets are important economically as navigation routes, and ecologically as conduits through which material flows from estuaries to the ocean.

Tidal forcing produces strong currents in inlets, with current speeds often >1 m s^{-1} in relatively narrow channels. During ebb tide, these jets can penetrate deeply (>1 km) onto the shelf. Within shallow inlets, the flows are generally vertically well mixed (unstratified), due to the large currents, and density gradients are assumed dynamically unimportant [e.g., *Hench and Luettich*, 2003]. Tidal inlet hydrodynamics can be affected by winds [*Geyer*, 1997] and waves [*Bruun*, 1978]. For example, near an inlet mouth, modeling studies show that wave-breaking-induced forces can be important in the momentum balance [*Bertin et al.*, 2009; *Malhadas et al.*, 2009; *Olabarrieta et al.*, 2011; *Dodet et al.*, 2013]. Modeling studies also show that incident waves affect the inlet ebb tidal jets [*Olabarrieta et al.*, 2014]. Recent observations at New River [*Wargula et al.*, 2014] and Katama Bay [*Orescanin et al.*, 2014] show that breaking-wave-driven along-inlet (cross-shore) radiation-stress gradients can be a substantial component of the along-inlet momentum balance. For large waves, these wave effects can significantly enhance flood flows and retard ebb flows.

Although within the inlet density gradients are not important dynamically, as the flow is vertically well mixed, stratification can be important offshore. For inlet water that is less dense (warmer or fresher) than the offshore ocean water, the ebb tide jet rides up and over the denser coastal ocean water as a "buoyant plume" [*Garvine*, 1999]. In a buoyant plume, the lighter fluid thins, spreads, and entrains deeper denser water, with entrainment and spreading linked [*Hetland and MacDonald*, 2008; *McCabe et al.*, 2008, 2009; *Chen et al.*, 2009]. There are few Lagrangian studies of plume spreading, and detailed model-data comparisons have not been performed. However, for a single drifter release at the Columbia River Mouth, gross

features of the observed and modeled drifters in the spreading plume compared well despite differences in individual trajectories [*McCabe et al*., 2009].

As inlets connect estuaries to the ocean, estuary-ocean exchange depends in part on tidal inlet hydrodynamics [*Liu et al*., 2008; *Malhadas et al*., 2010]. To quantify estuary-ocean exchange and to understand better the fate of pollution input into estuaries, estuarine residence times have been investigated. Although typically calculated using 2-D unstratified simulations of tidally forced circulation [*Bilgili et al*., 2005; *Yuan et al*., 2007; *Arega et al*., 2008; *Chen et al*., 2008; *de Brauwere et al*., 2011], residence times can depend on stratification [*Liu et al*., 2008] and wave [*Malhadas et al*., 2010] processes that often are neglected. In these studies, unstratified models were typically validated by comparing modeled and observed Eulerian currents within the estuary. Exchange, material transport, and dispersion are Lagrangian processes, hence models should be assessed from a Lagrangian perspective. However, Lagrangian model assessments are rare, although, within an estuary, individual modeled and observed drifter trajectories differed over 6 h [*Xu and Xue*, 2011]. At inlet mouths, detailed model-data Lagrangian comparisons have not been made.

As part of the RIVET-I experiment, a large Eulerian (current meter) and Lagrangian (drifter) data set was obtained at the New River Inlet, NC ("NRI") to study tidal inlet hydro and morphodynamics. As models are often used to analyze exchange, but are not well constrained by Lagrangian observations, here Lagrangian observations are compared with simulated drifter trajectories from two (NearCom and COAWST) numerical models providing a model-data comparison of tidal inlet flow from a Lagrangian perspective. This is in contrast to the majority of model validation studies which are from an Eulerian perspective [e.g., *Kumar et al*., 2015]. However, Eulerian model-data validations for the RIVET-I experiment using these models are in preparation: for NearCom see *Chen et al*. [2015] and for COAWST see M. Olabarrieta et al. (manuscript in preparation, 2015). As flows within inlets are vertically well mixed, stratification is neglected in both NearCom and COAWST. The validity of this assumption will be investigated using the observed and modeled drifter data sets.

The paper is organized as follows. A brief description of the experiment, including the bathymetry, instrumentation, and environmental conditions is provided in section 2. The models are described in section 3. Observed Lagrangian (drifter) and Eulerian (current meter) velocities are compared in section 4, and observed drifter velocities and spreading rates are presented in section 5. Observed and modeled Lagrangian statistics are compared in section 6. The differences between the observed and modeled Lagrangian statistics are discussed in regards to stratification (section 7), and the results are summarized in section 8.

2. New River Inlet Observations

Observations of tidal inlet flows were collected at the New River Inlet, North Carolina (NRI) during May 2012. This tidal inlet is on a barrier island that faces south east (Figure 1) with the community of Topsail on the south-west side of the inlet and the Marine Corps station Camp Lejeune on the north-east side of the inlet. A local coordinate system is chosen where the origin is in the inlet-mouth center, x increases offshore, and y increases to the northeast (58° from true, Figure 1). The inlet is approximately 1000 m wide at the mouth ($x = 0$ m) and narrows to 500 m wide approximately 500 m upstream of the mouth ($x = -500$ m). On 1–2 May, the inlet bathymetry was surveyed (for $-1000 < (x, y) < 1000$ m) on cross-shore lines with 50 m alongshore spacing. Surveyed bathymetry was interpolated to a regular grid (contours in Figure 1) and was smoothly embedded into an existing digital elevation model (with 10 m resolution) of the New River Inlet region. The inlet bathymetry shows four distinct features: (1) a large ebb tidal delta off the Topsail (south) side of the inlet, (2) the early April 2012 dredged "new" navigation channel adjacent to this shoal, (3) the previously dredged "old" navigation channel closer to Camp Lejeune, and (4) the narrow and deep (up to 11 m) channel that hugs the Topsail side of the inlet. In general, offshore of the inlet mouth (at $y = 0$), the bathymetry is shallow out to $x = 750$ m, after which the depth increases quickly offshore. South of the inlet mouth (for example at $y = -1000$ m), the depth increases more uniformly from the shore (Figure 1).

Instruments were deployed within and seaward of the inlet (see legend in Figure 1). Near the mouth of the inlet, depth-dependent currents were measured with 16 Acoustic Doppler Current Profilers (ADCPs) sampling once a minute, and near bottom currents were measured with 22 Acoustic Doppler Velocimeters (ADVs) sampling at 1 or 2 Hz. At all current meter locations, bottom pressure and temperature were also measured. A profiling wirewalker mooring measuring depth and time-dependent temperature and salinity

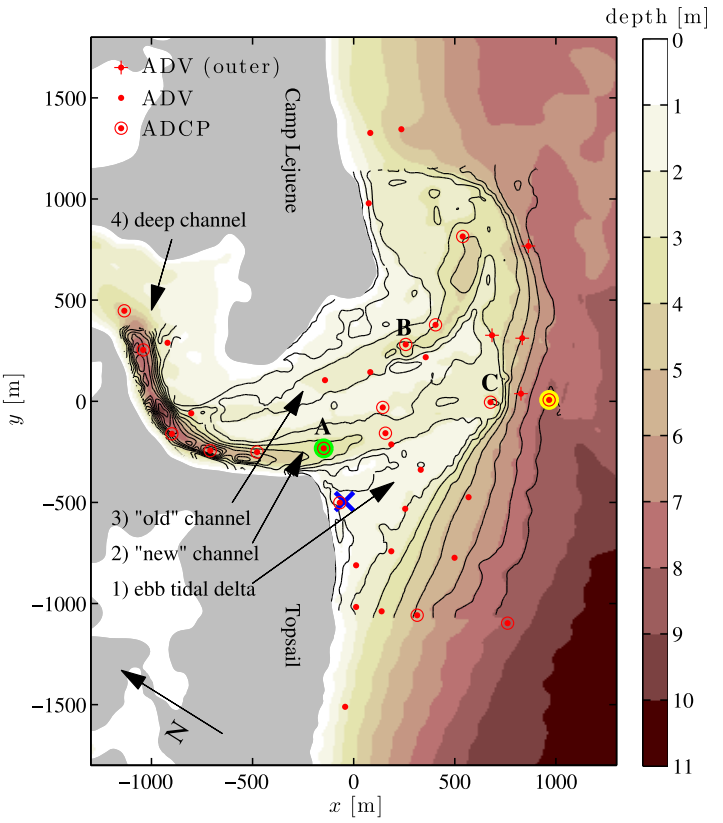

Figure 1. Plan view of the New River Inlet bathymetry as a function of cross-shore x and alongshore y coordinates. Depth is colored (scale on the right) and surveyed bathymetry is contoured (black curves) at 1 m intervals. Locations of instruments (red symbols, see legend in the top left), meteorological station (blue "x," $z = 4.3$ m), colocated ADCP and wirewalker ($(x, y) = (970, 0)$ m, yellow), and four prominent bathymetric features are indicated. The on/offshore velocity of the green colored ADCP ("ADCP0") is used to assess the tidal phase. Velocities at ADCPs "A," "B," and "C" are compared to model velocities in section 3.3.

was colocated with an ADCP 1000 m offshore of the mouth of the new channel in 8 m water depth (yellow in Figure 1). Wave heights and directions were obtained from a waverider buoy deployed by the U.S. Army Corp of Engineers Field Research Facility in 12 m water depth 6.1 km offshore of the inlet. Additionally, a meteorological station was installed on top of a piling positioned on the ebb shoal (at $(x, y) = (-100, -450)$ m, blue x in Figure 1).

GPS-tracked drifters [*Schmidt et al.*, 2003] were deployed repeatedly within and just seaward of the New River Inlet on 8 days between 1–4 and 14–17 May. Each of the 21 releases typically consisted of 34 drifters. There were 1–4 releases per day resulting in 68–328 drifter hours of observation each day. Releases are identified by the day and release number, e.g., d1r1 refers to the first release on 1 May and d5r2 refers to the second release on 14 May. Of the 21 total releases, 14 were during ebb tide, 4 were during flood, and 3 during slack. Here, six ebb releases are analyzed in detail and for these releases: (1) drifter initial locations were near the inlet mouth ($x \approx -500$ m, Figure 2a), (2) drifters completely exited the inlet, and (3) maximum ebb tidal velocities were similar (Figure 3a). Although the ebb velocities are similar, the 14–17 May ebb releases are not analyzed in detail because release locations were farther upstream ($x < -1000$ m) and many drifters did not exit the inlet. For the six ebb releases examined here, the 34 drifters were deployed within approximately 100 m of each other over 5 min, resulting in a unique initial time and position for each drifter.

The drifters were 0.5 m tall [*Schmidt et al.*, 2003] and rarely encountered the bottom. Drifter tracks were quality controlled to exclude data contaminated by dragging. For each quality controlled drifter track, colocated drifter position $\vec{X}(t)$ and velocity $\vec{u}_L(t)$ time series are derived from 1 Hz GPS positions $\vec{X}(t) = (X(t), Y(t))$, as $[\vec{X}(t+dt) + \vec{X}(t)]/2 \rightarrow \vec{X}(t)$ and $[\vec{X}(t+dt) - \vec{X}(t)]/dt \rightarrow \vec{u}_L(t)$. Absolute position errors are $\approx \pm 2$ m, but vary slowly in time and result in relatively small errors in drifter relative position and velocity [*Schmidt et al.*, 2003]. Drifter wind slip, estimated as roughly 1% of the wind speed [*Schmidt et al.*, 2003] is not accounted for. The drifters also measured near-surface water temperature.

During the 21 drifter releases, a range of tide, wind, and wave conditions were encountered (Figure 3). Depth-averaged cross-shore velocity u_E near the inlet-center $(x, y) = (-150, -230)$ m (green in Figure 1, denoted ADCP0) generally varies between -0.5 m s^{-1} (flood) and $+1.0$ m s^{-1} (ebb) (Figures 3a and 3b). Thus, on 1 May, the first and second releases (dark shading in Figure 3a) were during ebb tide and the third release was during flood tide (light shading). The six ebb releases analyzed here, where drifters were released close to the inlet mouth and exited the inlet, are indicated by dark shading. The remaining 15 releases are indicated by light shading and are not analyzed in detail. Seven of these releases were also ebb tide releases (e.g., d5r1),

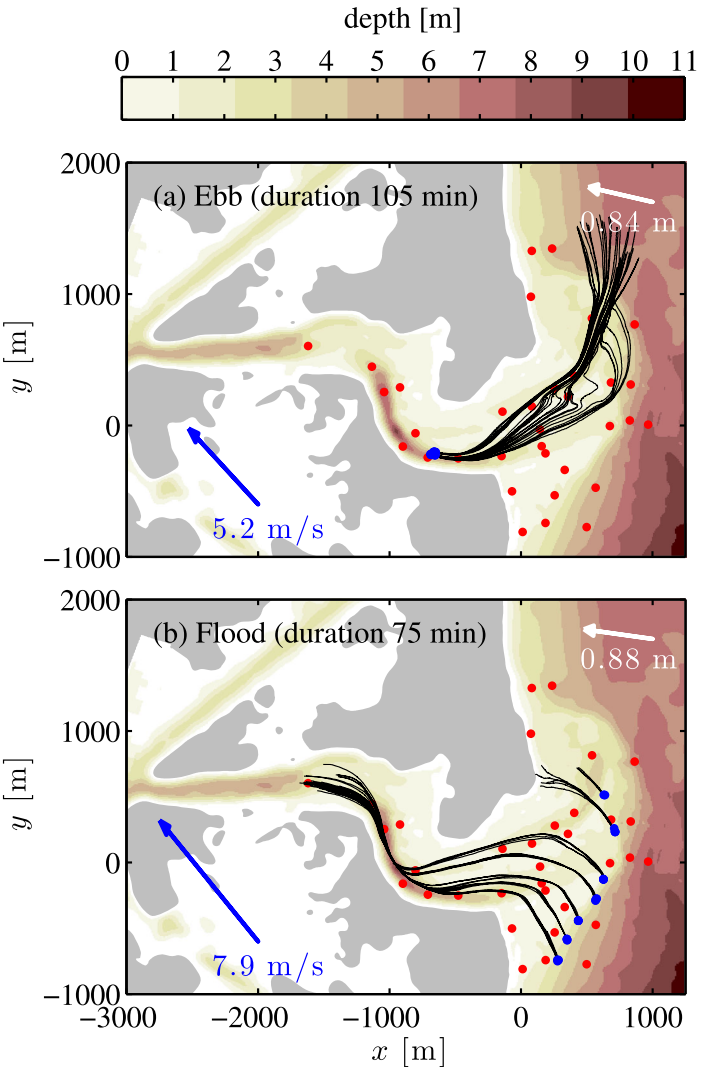

Figure 2. Example trajectories for a typical (a) ebb release (d1r2) and (b) flood release (d1r3). Initial drifter locations are blue dots and fixed instrument locations are red dots. Water depth is colored (scale at top). Release-averaged wind vectors are dark blue arrows (lower left) and wave properties (significant wave height and direction) are in white (upper right). Red dots are current meter locations.

but had initial drifter locations far upstream of the inlet mouth and drifters did not completely exit the inlet. The remaining eight releases were during either flood (e.g., d1r3) or slack tide (e.g., d2r2).

Wind speeds during drifter releases were 1–9 m s^{-1} (Figures 3c and 3d) and were from approximately −45° (in experiment coordinates) on d1,2,3,4,6,7; approximately onshore (0°) on d5; and from −200° on d8 (Figures 3e and 3f). At the offshore buoy, significant wave heights were 0.5–1.3 m (Figures 3g and 3h) with mean directions from approximately −15° on d1,5,6,7,8; from 0° on d3 and d4r3,4; from 10° on d2; and from 40° on d4r1,2 (Figures 3h and 3i). Peak wave periods were 5–8 s (not shown).

3. Models

Observed drifter trajectories are simulated by two models, COAWST and NearCom, that simulate currents forced by waves, winds, and tides. In both models, wave-current interactions are included, and the effects of stratification are neglected. Both models use the wave generation and propagation model SWAN (Simulating WAves in the Nearshore [*Booij et al.*, 1999]), with frequency resolution $\Delta f = 0.025$ Hz and directional resolution 6°. The circulation models and SWAN are forced with 5 min wind and atmospheric pressure observations at the meteorological station (blue x in Figure 1), assumed spatially uniform. Both models are forced on the boundary by tides with tidal constituents provided by the ADCIRC database. Model grids are generated from a high-resolution bathymetric survey near the mouth (from 11 May 2012) and a larger domain digital elevation model (Figure 1).

3.1. COAWST

The coupled ocean-atmosphere-wave-sediment-transport modeling system (COAWST) [*Warner et al.*, 2010; *Olabarrieta et al.*, 2011] used here includes SWAN and an ocean model ROMS (Regional Ocean Modeling System) [*Shchepetkin and McWilliams*, 2005; *Haidvogel et al.*, 2000, 2008]. ROMS is a three-dimensional, free-surface, terrain-following numerical model that solves finite-difference approximations of the Reynolds-averaged Navier-Stokes (RANS) equations using the hydrostatic and Boussinesq assumptions [*Haidvogel et al.*, 2000; *Chassignet et al.*, 2000]. Wave-averaged momentum balance equations [*McWilliams et al.*, 2004; *Uchiyama et al.*, 2010] are implemented in the COAWST modeling system [*Kumar et al.*, 2012]. A detailed description of the modeling system can be found in *Kumar et al.* [2012]. For this experiment,

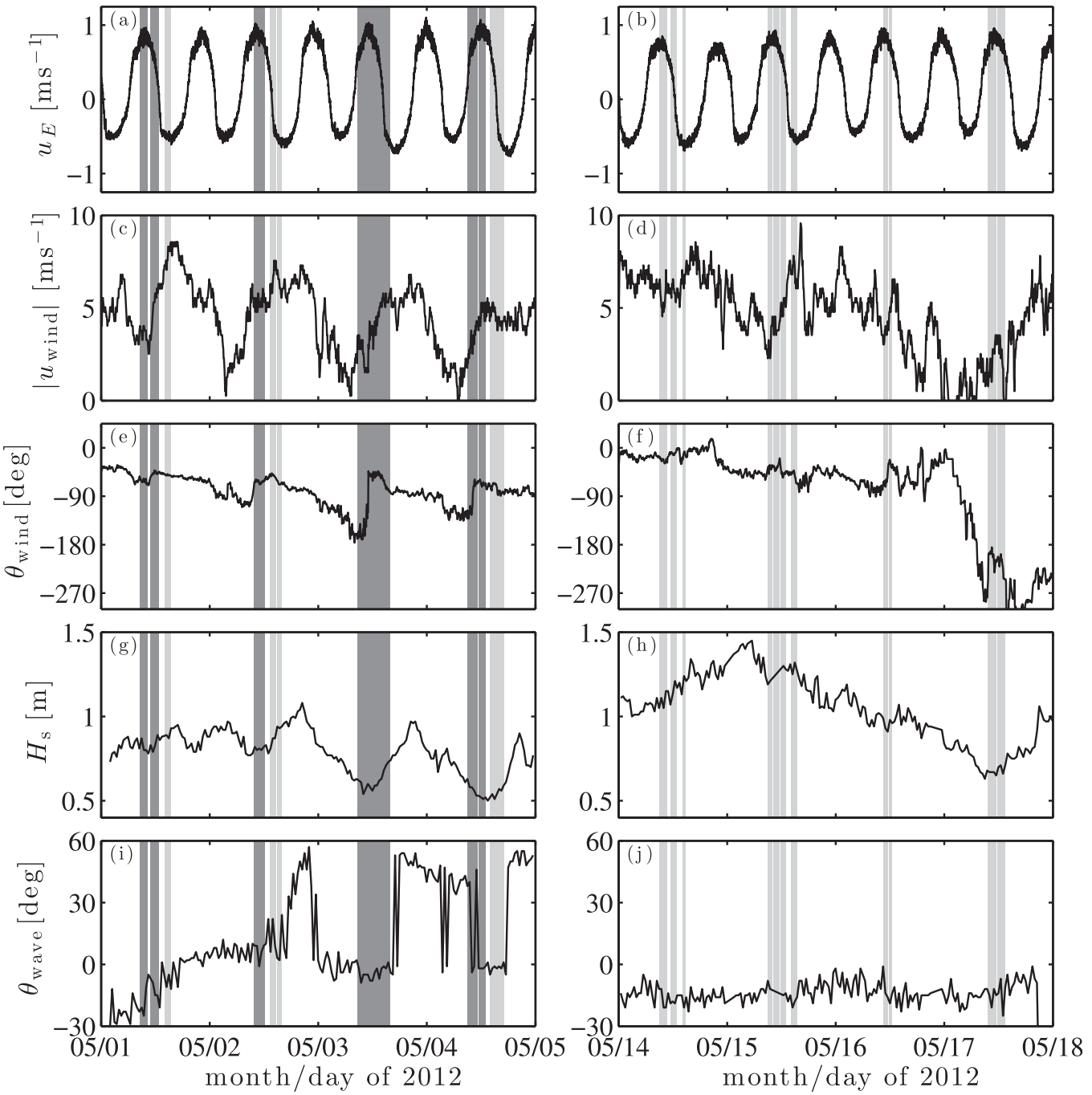

Figure 3. Environmental conditions versus time, (left column) 1–5 May 2012 and (right column) 14–18 May 2012: (a and b) depth-averaged cross-shore ADCP velocities u_E near the inlet mouth (green dot in Figure 1), (c and d) wind speed $|u_{\mathrm{wind}}|$, (e and f) wind direction θ_{wind}, (g and h) incident significant wave height H_s, and (i and j) wave direction θ_{wave} in degrees relative to normal incidence. Drifters were released during the 21 shaded intervals with the six ebb releases analyzed in detail indicated by darker shading.

Olabarrieta et al. (manuscript in preparation) provide extensive comparisons of COAWST with waves and currents measured with the fixed instruments.

SWAN and ROMS models used the same, nested horizontal curvilinear grids. The parent grid, with 60 m average resolution, spans 50 km in the cross shore from the upper limit of the estuary to 15 km offshore ($\approx$ 25 m water depth), and at the inlet mouth spans 22 km alongshore. The child grid is centered at the inlet ($(x, y) = (0, 0)$ m) spanning approximately 7 km in the cross shore and 8 km in the alongshore with 10–15 m grid resolution. ROMS parent and child grids used five equally spaced sigma vertical layers. SWAN boundary

conditions were derived from the NOAA database of operational output (WAVEWATCH III version 2.22 hindcast). In ROMS, tidal forcing propagates along the boundary. The coupled ROMS-SWAN hindcast simulations were run from 1 to 21 May 2012.

3.2. NearCom

New River Inlet hydrodynamics were also modeled [*Chen et al*., 2015] using NearCom-TVD [*Shi et al*., 2003], which couples SWAN [*Booij et al*., 1999] and a curvilinear quasi-3-D nearshore circulation model SHORECIRC [*Svendsen et al*., 2004]. SHORECIRC is a two-dimensional horizontal (2-DH) model that incorporates the mixing effect induced by the vertical variation of wave-induced horizontal circulation [*Putrevu and Svendsen*, 1999]. For a well-mixed coastal environment with negligible baroclinic gradients, quasi-3-D models are similar to full 3-D circulation models [*Haas and Warner*, 2009]. In some applications, the computational efficiency of NearCom relative to depth-resolving models is advantageous.

NearCom model resolution varies and is similar to COAWST resolution with 10 m resolution in the inlet mouth and about 200 m resolution offshore and in the backbay area. SWAN boundary conditions (significant wave height and peak period) were derived from NOAA buoy 41036 (25 m depth, 46 km offshore), but due to missing data at this buoy, mean wave direction is from the waverider buoy (12 m depth, 6.1 km offshore). In NearCom, the tidal forcing is constant at any time along the boundary, and thus does not propagate. The NearCom model setup and comparison with fixed instruments are presented in *Chen et al*. [2015].

3.3. Eulerian Velocity Model-Data Comparison

Comprehensive model-data comparisons of Eulerian velocities for NearCom [*Chen et al*., 2015] and COAWST (Olabarrieta et al., manuscript in preparation, 2015) are presented elsewhere. However, prior to a more detailed Lagrangian drifter model-data comparison, a limited Eulerian velocity model-data comparison, spanning the six analyzed ebb releases on 1–4 May, is performed at three ADCP locations within the inlet, within the old channel, and at the seaward edge of the ebb shoal (denoted A, B, and C, respectively in Figure 1). At each ADCP, the observed velocities are rotated into velocity principle axes (which generally coincide with the local bathymetry contours, Figure 1) with major axis U_p and minor axis U_m velocities (black curves Figure 4) that have rotation angles $\theta_r = 15°$, 22°, and 12° counterclockwise from $+x$ for A, B, and C, respectively. COAWST and NearCom model velocities are also rotated into the observed principal axis coordinate.

Observed velocity (black curves Figure 4) is largest within the inlet (location A) and smaller farther offshore (location C). At location A, observed principal-component tidal velocity U_p (black curve Figure 4a) is $\approx 1\,\mathrm{m\,s^{-1}}$ at maximum ebb and $\approx -0.5\,\mathrm{m\,s^{-1}}$ during maximum flood and is largely semidiurnal. At location B, observed U_p has similar maximum ebb velocity as location A, but smaller ($U_p \approx -0.25\,\mathrm{m\,s^{-1}}$) maximum flood velocities. Farther offshore at the seaward edge of the ebb shoal (location C), observed U_p maximum ebb ($\approx 0.5\,\mathrm{m\,s^{-1}}$) and flood ($\approx -0.1\,\mathrm{m\,s^{-1}}$) velocities are weaker than at instruments A and B. Observed minor axis velocities U_m (black curves Figures 4d–4f) are smaller than U_p and have little tidal signal. In addition, during the ebb drifter releases (dark gray shading in Figure 4), at all three locations, the observed $U_m > 0$ indicating $+y$ flow during ebb tide (recall the rotation angle is small).

At these three locations, modeled and observed velocities show similarities and differences (Figure 4). In particular, the observed and modeled principal axis velocities U_p have similar magnitudes and phases (Figures 4a–4c), except that the COAWST U_p magnitude at A is larger than observed, and observed ebb tide U_p is larger than COAWST and NearCom at B (and to a lesser extant at C). At locations A, B, and C, the model-data root-mean-square U_p error is 0.15 (0.19), 0.27 (0.24), and 0.14 (0.20) $\mathrm{m\,s^{-1}}$, respectively, for COAWST (NearCom). At location A, NearCom model U_p errors are larger because the modeled flood to ebb transition leads the observations by ≈ 1 h (Figure 4a). Although the observed minor axis velocity U_m have little tidal signal, the COAWST and NearCom modeled U_m have a tidal component at location A (red and green curves in Figure 4d), indicating that modeled principal axes are $\approx 8^{\circ}$ off of the observed principal axis. At location B in the old channel, modeled and observed U_m are similar (Figure 4e). However, at the seaward edge of the ebb shoal (location C) modeled, U_m is less than observed.

3.4. Modeled Drifter Tracks

NearCom provides depth-average Lagrangian velocities $\vec{u}_{L,\mathrm{m}}$ that are the sum of mean Eulerian velocities $\vec{u}_{E,\mathrm{m}}$ and Stokes drift $\vec{u}_{S,\mathrm{m}}$, i.e., $\vec{u}_{L,\mathrm{m}} = \vec{u}_{E,\mathrm{m}} + \vec{u}_{S,\mathrm{m}}$. Stokes drift velocities are relatively small in both NearCom and COAWST. COAWST provides depth-dependent velocities and the mean surface Lagrangian velocities

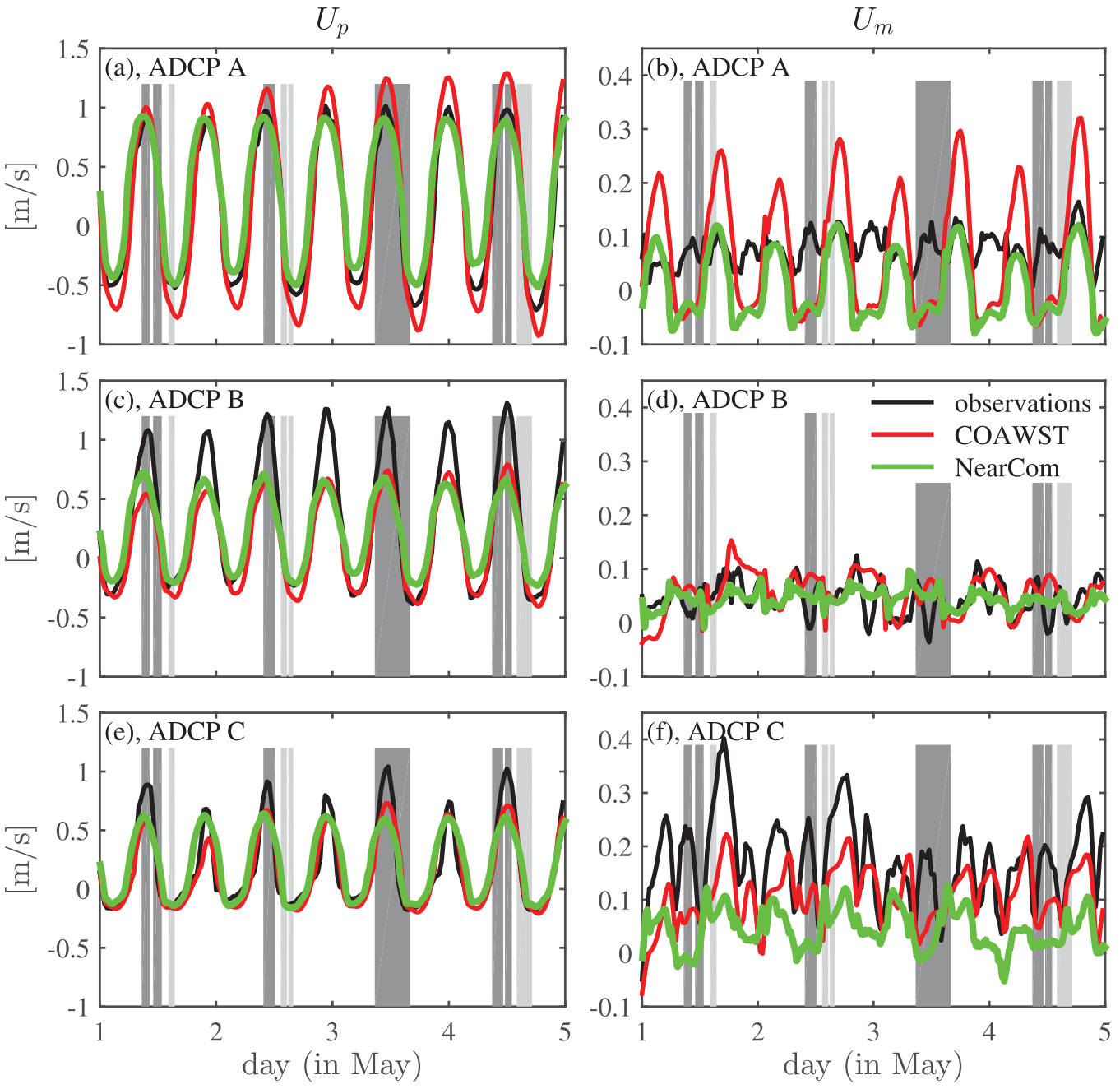

Figure 4. Modeled (red and green) and observed (black) depth-averaged velocities for the first 2 days of May at three ADCPs (A, B, and C, see Figure 1). Modeled and observed velocities are in observed velocity principle axis coordinates (at angles 15°, 22°, and 12° counterclockwise from $+x$ for A, B, and C, respectively). (a, c, and e) Principle axis velocities U_p are positive out of the inlet and (b, e, and f) minor axis velocities U_m are positive 90° left of positive U_p. Gray shading indicates drifter release times with dark shading indicating ebb releases.

are used to advect modeled drifters, however, results are not sensitive to using depth-averaged COAWST velocities. Modeled drifter trajectories $\vec{X}_\mathrm{m}$ are obtained by offline integration of

$$\vec{X}_\mathrm{m}(t)=\vec{X}_\mathrm{m}(t=0)+\int_0^t [\vec{u}_{L,\mathrm{m}}(\vec{X}_\mathrm{m}(t'),t')+w(t')]\,dt', \tag{1}$$

where (1) is discretized with a forward Euler step. Model velocities are spatially linearly interpolated to model drifter positions, because modeled drifter positions are not at model grid points. Although (1) is only first-order accurate in time, modeled drifter paths would not differ substantially if a higher-order method were used as the time step $\Delta t=2$ s used is small compared to both the time scale over which the currents

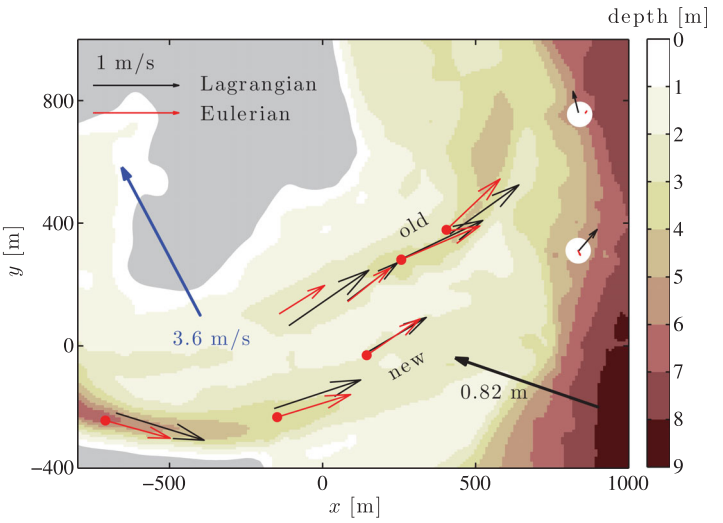

Figure 5. Drifter-mean Lagrangian $\vec{U}_L$ (thin black arrows) and Eulerian $\vec{U}_E$ (red arrows) velocities for d1r1. ADV velocities are red arrows without dots and ADCP velocities are depth averaged and indicated by red arrows with red dots. The bathymetry is colored (scale at right). The wind direction and magnitude are indicated in blue, and the wave direction and significant wave height are indicated in black (bottom right).

are changing (tidal) and the advective time scale $L/U \approx 1000$ s, where L is the length scale over which velocities change in the direction of U. Sufficient to resolve the tidal flows, modeled velocity fields $\vec{u}_{L,\mathrm{m}}$ are separated by 10 and 5 min for COAWST and NearCom, respectively, and linearly interpolated in time in the time stepping procedure. For each drifter track, the modeled initial drifter positions $\vec{X}_{\mathrm{m}}(t=0)$ are equal to the observed drifter release location, and the subsequent trajectory durations are equal. Thus, all 34 observed and modeled drifter tracks are unique, even though modeled drifter releases have the same number, initial positions, and durations as the observed drifters. To represent turbulent processes not resolved by the models, and to better match the higher-frequency observed Lagrangian velocities, weak horizontal diffusion, equivalent to $\kappa = 0.1\,\mathrm{m^2\,s^{-1}}$, is added to each trajectory by including the random Weiner process $w(t')$ [e.g., *Berloff and McWilliams*, 2002]. The sensitivity of modeled drifter tracks to the value of κ was explored, and the results presented here do not depend on κ as long as $\kappa \leq 0.1\,\mathrm{m^2\,s^{-1}}$. Model drifters that would cross a land boundary are reflected back into the fluid, conserving drifters.

4. Comparison of Observed Lagrangian With Eulerian Velocities

At NRI, the observed drifters often closely passed (within < 50 m) current meters (see Figure 2) providing an opportunity to directly compare Lagrangian (drifter) with Eulerian (current meter) velocities. For each release, the drifter-mean Lagrangian velocity $\vec{U}_L = (U_L, V_L)$ at a current meter is defined as the average of all drifter velocities $\vec{u}_L(t)$ for all drifters that passed within 50 m of a current meter. Thus, multiple drifters that pass the same current meter can contribute to $\vec{U}_L$. The results do not change appreciably for radii between 25 and 100 m. The drifter-mean Eulerian velocity $\vec{U}_E = (U_E, V_E)$ is calculated as the time average of the current meter velocities $\vec{u}_E(t)$ over the times that drifters were within 50 m of the current meter. In calculating the drifter-mean Eulerian velocity time-average, times are weighted by the number of drifters that pass the current meter. For example, if three drifters passed by a current meter for the times $t_0 < t < t_1$, this time period is given triple weight in the average. Drifter-mean Lagrangian $\vec{U}_L$ and Eulerian $\vec{U}_E$ velocities are calculated at each current meter that drifters closely passed for all 21 drifter releases.

Before comparing drifter-mean Lagrangian with Eulerian velocities for the entire experiment, a single release is examined. For the d1r1 release, drifter-mean Lagrangian $\vec{U}_L$ and Eulerian $\vec{U}_E$ velocities compare well within the inlet (black and red arrows in Figure 5), even at the deepest ($h \approx 8$ m at $(x, y) \approx (-800, -300)$ m) current meter within the inlet channel. Consistent with boundary layer flow, the surface sampled drifter velocities ($|\vec{U}_L|$) are usually only a little larger than the near-bed (ADV) or depth-averaged (ADCP) current meter velocities ($|\vec{U}_E|$), suggesting the flow within the inlet is mostly vertically uniform but slightly larger at the surface.

At the outer-edge of the ebb-tidal shoal, $\vec{U}_L$ and $\vec{U}_E$ compare poorly (white circles in Figure 5, $h \approx 4$ m), where $|\vec{U}_L|$ is small and $|\vec{U}_E|$ is near zero, suggesting that surface and near-bottom velocities can differ significantly at the outer limit of the inlet mouth. Surface Stokes drift velocities and surface horizontal velocity

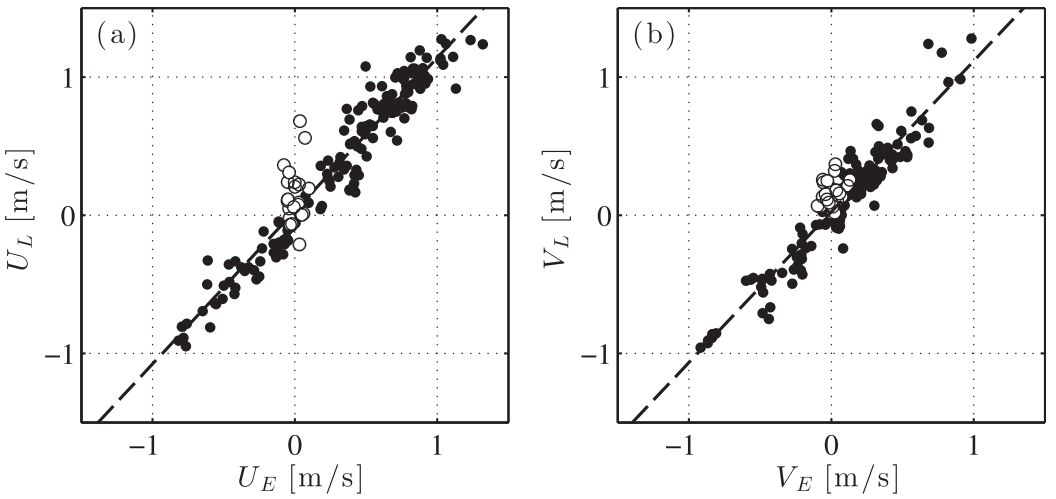

Figure 6. Drifter-mean Lagrangian versus drifter-mean Eulerian velocities: (a) cross-shore U_L versus U_E, and (b) alongshore V_L versus V_E. Dashed lines are linear best fits to the 183 points with slopes of 1.06 for U (R_U^2=0.92) and 1.05 for V (R_V^2=0.94). Open circles are values for the ADVs at the outer-edge of the ebb-tidal shoal (red pluses in Figure 1).

gradients could contribute to this difference between drifter-mean Lagrangian and Eulerian velocities, however, these factors are too small to explain the large difference indicated in Figure 5.

Consistent with the d1r1 release (Figure 5), $\vec{U}_L$ and $\vec{U}_E$ are also similar for all 21 releases (183 total velocities) in both velocity components U and V (Figure 6). An exception to the usually good agreement is at the outer-edge of the ebb-tidal shoal (red $+$s in Figure 1) where U_E (and V_E) is near zero, but U_L (and V_L) is not always small (open circles in Figures 6a and 6b). Using all data points, the square correlation (R^2) between the drifter-mean Lagrangian and Eulerian velocities is high for both cross-shore (R_U^2=0.92, Figure 6a) and alongshore (R_V^2=0.94, Figure 6b) components and rms errors are 0.17 and 0.13 m s^{-1} for U and V, respectively. The best fit slopes indicate $\vec{U}_L \approx 1.05\,\vec{U}_E$ (dashed lines in Figures 6a and 6b), consistent with the d1r1 faster (surface) $|\vec{U}_L|$ than (near bed or depth average) $|\vec{U}_E|$. Thus, within the inlet, drifters and current meters are sampling the same nearly vertically uniform boundary layer flow field that is slightly surface intensified. For the small waves during the drifter releases, Stokes drift velocities (calculated using linear theory) are small ($O(0.01)$ m s^{-1}), and thus do not affect U_L.

5. Ebb Lagrangian Observations

Observations of drifter trajectories, velocities, and cluster spreading statistics are discussed for six ebb releases where drifters transitioned from the inlet to the shelf, similar to previous studies at larger systems [*McCabe et al*., 2008; *Hetland and MacDonald*, 2008].

5.1. Drifter Paths and Velocities

Drifter velocities $\vec{u}_L$ are spatially binned (50 by 50 m bins) by drifter positions $\vec{X}_L$ to derive surface mean velocity maps for each release. Velocities range between 1.25 m s^{-1} in the channels to near zero offshore. Flow patterns are generally similar for the six releases (Figure 7), as expected given the similar release locations and tidal phase. Drifters exit the inlet preferentially through either the new or old channels (see Figure 1). After passing through the relatively narrow channels, velocity magnitudes decrease as drifters move into the deeper coastal-ocean waters offshore of the ebb tidal shoal (as in *Hetland and MacDonald* [2008]). Offshore of the ebb shoal, the drifters turn leftward and advect in the $+y$ direction, perhaps due in part to the $+y$ wind component present on all releases (blue arrows in Figure 7) or to the $+y$ wave component present on two releases (green arrows in Figures 7a and 7b).

The d1r1, d2r1, and d4r2 velocity magnitude maps (Figures 7a, 7b, and 7f) are nearly synoptic as inlet tidal velocities (Figure 3a) did not change significantly over the duration ($<$ 2 h) of the release, similar to maximum ebb at other locations [*Hetland and MacDonald*, 2008] and consistent with momentum balances at tidal inlets in which local accelerations (du/dt) are small during maximum ebb [*Hench and Luettich*, 2003].

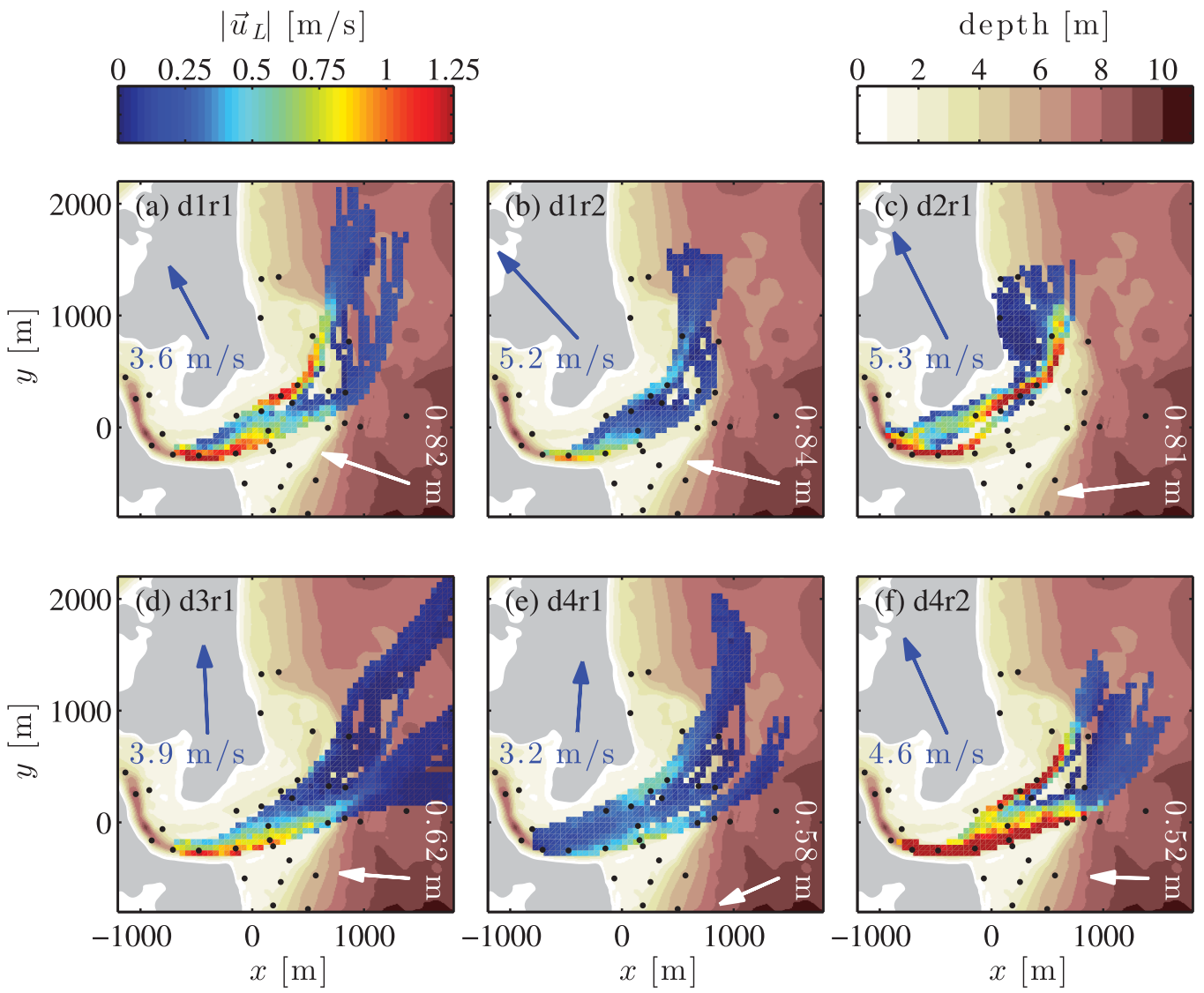

Figure 7. Spatially binned (in 50 by 50 m bins) Lagrangian velocity magnitude (colored blue to red, scale in upper left) over the bathymetry (colored white to brown, scale in upper right) for the six ebb releases: (a) d1r1 to (f) d4r2. Current meter locations (black dots), wind direction θ_{wind}, and magnitude $|u_{\text{wind}}|$ (blue), wave direction θ_{wave}, and significant wave height H_s (white), are indicated. Black dots are current meter locations.

The d3r1 velocity map (Figure 7d) is also synoptic across the ebb tidal shoal ($x < 1000$ m) as drifters passed through this region quickly due to the large velocities (>0.3 m s^{-1}) in this region.

5.2. Spreading

To prevent falsely assigning dispersion to drifters exiting through different channels, clusters of drifters are considered separately. Specific drifter clusters exited through either the old channel or the new channel (Figures 2a and 7). For example, d1r1 (Figure 7a) has two obvious clusters, d1r1-new and d1r1-old, corresponding to new and old channel exits, respectively. For the six ebb releases, there are 1–2 clusters per release and a total of 11 drifter clusters including 5 that exited the new channel and 6 that exited the old channel.

For each cluster, the cluster center of mass is

$$\vec{X}_c(t) = \langle \vec{X}(t) \rangle, \tag{2}$$

where $\vec{X}(t)$ is the drifter position and averaging, denoted by $\langle\rangle$ is over all drifters in the cluster. The cluster velocity is then

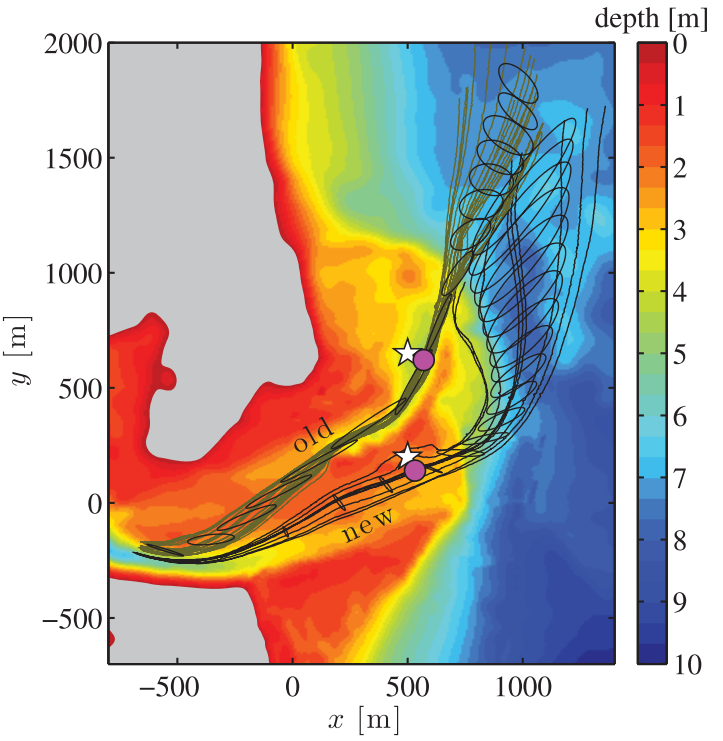

Figure 8. Drifter tracks for the d1r1 release superposed on bathymetry (colors, scale on right). Green (black) drifter tracks exited the old (new) channel. Standard deviation ellipses, with principle and minor axis lengths $a(t)$ and $b(t)$, respectively, about the cluster center of mass $\vec{X}_c(t)$ are shown every 5 min. The critical point separating inner and outer inlet regions along a cluster track (magenta dots) is defined in reference to $(x_0, y_0)=(500,\ 200)$ m and (500, 650) m for the old and new channel clusters, respectively (white stars).

$$\vec{U}_c(t)=\frac{d}{dt}\vec{X}_c(t)\,. \tag{3}$$

The cluster cloud size is found by calculating the drifter position covariance matrix D_{ij}

$$D_{ij}(t)=\langle X_i(t)X_j(t)\rangle-X_{c,i}(t)X_{c,j}(t), \tag{4}$$

where i and j refer to direction. At every t, the position covariance matrix D_{ij} is diagonalized to obtain the major $a(t)$ and minor $b(t)$ axes, and the angle α that the principle axis makes with the $+x$ axis.

Drifter cluster cloud ellipses centered at $\vec{X}_c(t)$, for both of the d1r1 clusters are shown in Figure 8. The d1r1 old channel cluster (d1r1-old, green tracks in Figure 8) shrinks as it enters the old channel and then grows rapidly upon entering deeper water (at $(x,y)\approx(600,600)$ m). The d1r1-new cluster cloud (black tracks in Figure 8) also grows rapidly upon entering deeper water (at $(x,y)\approx(750,\ 200)$ m).

The cluster spreading rate μ, defined as

$$\mu=\frac{1}{2}\frac{d}{dt}D, \tag{5}$$

where $D(t)=a(t)b(t)$ is related to the drifter ellipse area A, $A=\pi D$, is calculated for each cluster and smoothed in time with a 3 min low-pass filter. For all releases, cluster spreading rates μ (Figure 9) indicate that spreading $\mu>0$ (red colors) occurs when drifters enter deeper water ($x>500$ m) in contrast to near-zero μ in regions within the inlet. Spreading rates μ also indicate that old channel drifter clusters (upper tracks in each panel) often contract in the old channel ($\mu<0$ in Figures 9a, 9c, 9e and 9f) before expanding (see Figure 8). For the drifter clusters exiting the new channel, the spreading rate is more variable between releases. However, large positive spreading rates for new channel exits are found when drifters enter deeper shelf waters for d1r1, d3r1, and d4r2 (Figures 9a, 9d, and 9f).

The offshore increase in μ is quantified by averaging μ over distinct inner and outer inlet regions. The boundary between inner and outer inlet regions (x_0, y_0) for the new and old channels, $(x_0, y_0)=(500, 200)$ and (500, 650) m, respectively (stars in Figure 8), is where the channel width begins to increase and the channels become less well defined. As clusters do not exactly pass (x_0, y_0), the cluster location closest to (x_0, y_0) is taken as the transition from inner to outer inlet (magenta dots in Figure 8). Averaged over all 11 clusters, the average inner-inlet spreading rate $\mu_{\text{in}}=0.5\,\text{m}^2\,\text{s}^{-1}$ is smaller than the outer inlet spreading rate $\mu_{\text{out}}=2.8\,\text{m}^2\,\text{s}^{-1}$.

Cluster velocities $|\vec{U}_c|$ and spreading rates μ vary with downchannel distance l from (x_0, y_0) (Figure 10). For d1r1 (Figure 7a), $|\vec{U}_c|$ decreases linearly with l until a roughly constant $\approx 0.25\,\text{m}\,\text{s}^{-1}$ is reached at $x=1000$ m in both the new and old channels (grey dashed lines in Figures 10a and 10b). For the new channel cluster, $|\vec{U}_c|$ is maximum at the release location (Figure 10a), whereas for the old channel, $|\vec{U}_c|$ is maximum downstream of the release location (Figure 10b). A linear dependence of $|\vec{U}_c|$ on l (constant $d|\vec{U}_c|/dl$)

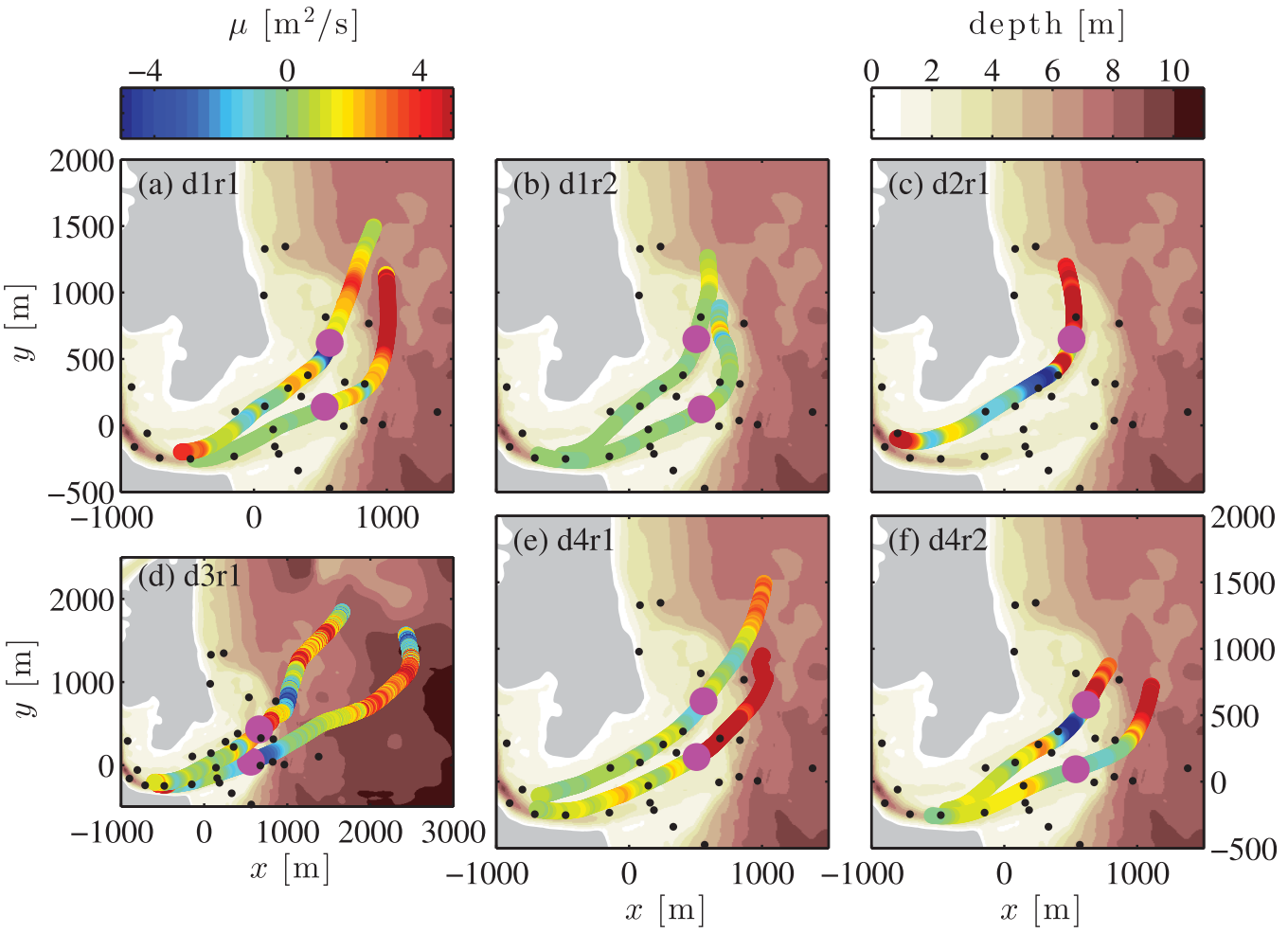

Figure 9. The cluster spreading rate μ (colored blue to red, scale on upper left) for the six ebb releases on the cluster trajectory $\vec{X}_c(t)$. Bold magenta dots separate inner and outer regions. The axis limits in Figure 9d are larger than the other plots. White to brown colors are bathymetry (scale on upper right). Black dots are current meter locations.

is found for all 11 clusters. A linear best fit for the 700 m span downstream of the $|\vec{U}_c|$ maximum yields average new channel $d|\vec{U}_c|/dl = -4.6\times10^{-4}\ s^{-1}$ and old channel $d|\vec{U}_c|/dl = -5.1\times10^{-4}\ s^{-1}$ decelerations.

The relationship between cluster spreading and cluster velocity as drifters move onto the shelf is similar to plume spreading where cluster (plume) velocities decrease downstream while cluster (plume) widths increase downstream [*McCabe et al.*, 2008]. However, the present decelerations $d|\vec{U}_c|/dl \approx -5\times10^{-4}\ s^{-1}$ are larger than those reported for the Columbia River Mouth ($\approx -1\times10^{-4}\ s^{-1}$) [*McCabe et al.*, 2008].

6. Comparison of Observed and Modeled Drifters: Trajectories, Velocities, and Spreading

For the 34 drifters of the d1r1 release (similar to other ebb releases, Figure 7), observed and modeled trajectories have similarities and differences (Figure 11). A much larger fraction of observed drifters (black in Figure 11) take the old channel exit path than the modeled (red and green in Figure 11) drifters, which preferentially exit the new channel (see Figure 1 for orientation). The difference between observed and modeled paths originates near the release location (star in Figure 11), with observed drifters heading to the left (toward $+y$) approximately 500 m from the release location, a feature not present in the model trajectories. This difference is due to weaker modeled than observed cross-channel velocity (v) in this region during ebb tide. In this region during the ebb drifter releases (dark gray shading Figure 4b), observed cross-channel flow (U_m) is positive (toward Camp Lejuene), whereas modeled cross-channel flow is negative. It is

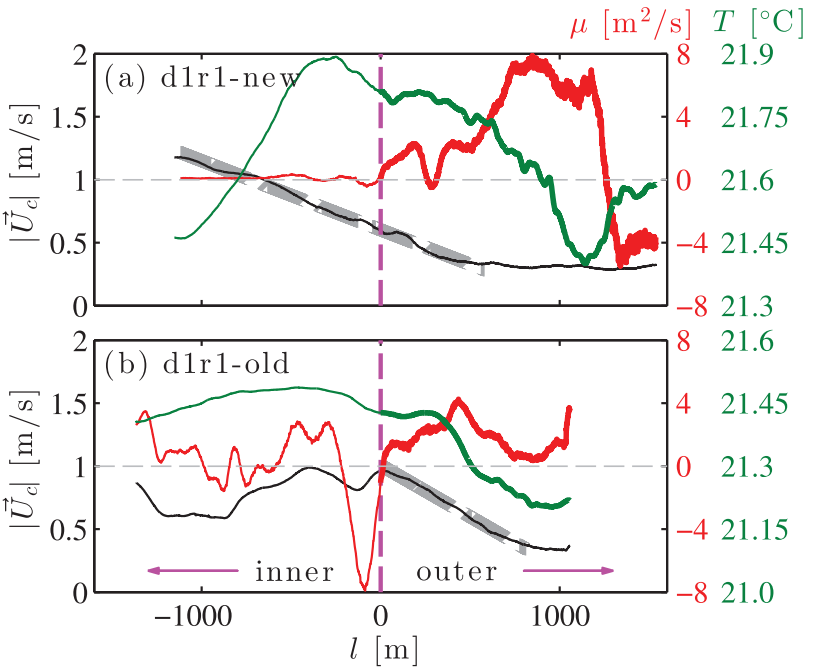

Figure 10. The cluster velocity magnitude (black), spreading rate (red), and temperature (green) versus downstream distance l, with $l = 0$ separating inner and outer regions, for (a) a new channel cluster exit d1r1-new and for (b) an old channel cluster exit d1r1-old. The decelerating $|U_c|$-l best fit lines are indicated by thick dashed gray lines. Spreading rates and temperatures for $l < 0$ are thin curves (i.e., μ_{in}) and for $l > 0$ are thick curves (i.e., μ_{out}).

not known why the models do not reproduce the observed cross-channel flow in this region. However, observed and modeled differences in the cross-channel flow in this region may be related to weaker modeled velocities in the old channel (Figure 4c). Thus, weaker modeled old channel flow may be responsible for fewer modeled drifters exiting the old channel. The few observed (black) and many COAWST (red) modeled drifters that exit the new channel take a sharp left turn upon entering deeper waters near $(x, y) \approx (750, 200)$ m. In contrast, NearCom (green) modeled new channel exiting drifters move straight offshore. Observed, COAWST, and NearCom drifter path differences may be due to model boundary conditions, imperfect bathymetry, model resolution, and assuming spatially homogeneous winds. However, better COAWST than NearCom drifter paths may indicate that resolving the vertical structure of the flow at the inlet mouth may be critical to drifter exit paths or that including progressive tidal propagation on the boundaries is important as tidal forcing is progressive in COAWST but standing in NearCom. Inlet flows and their symmetry depend on whether offshore tides propagate progressively with

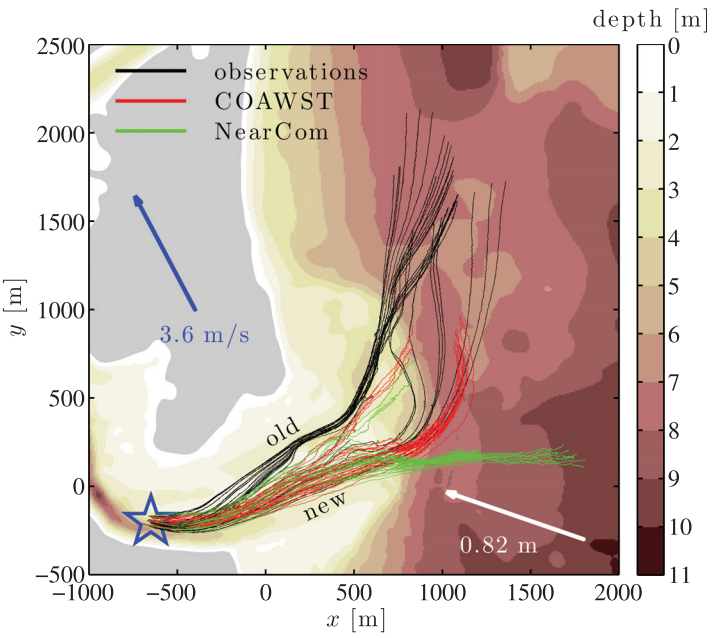

Figure 11. All observed (black), COAWST (red), and NearCom (green) drifter tracks for the d1r1 release. Initial drifter locations are near the blue star. Observed wind magnitude and direction (blue) and significant wave height and direction (white) are indicated. White to brown colors are bathymetry (scale on the right).

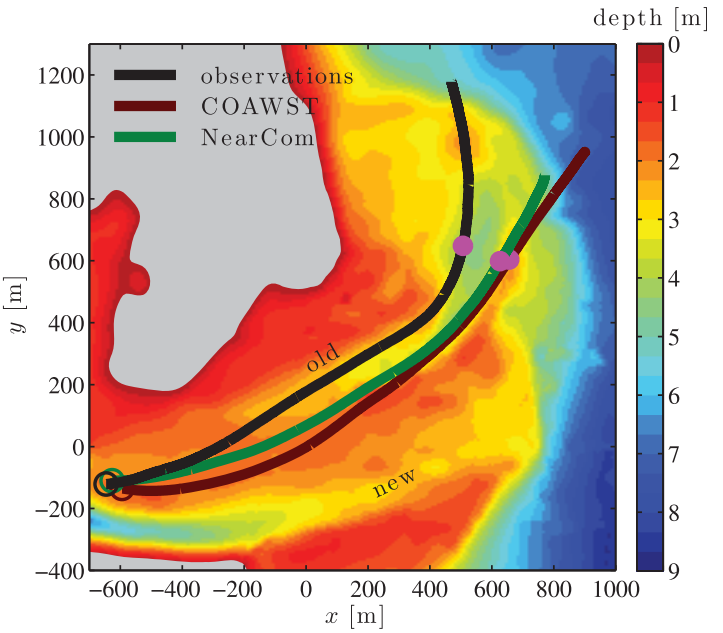

Figure 12. The d2r1-old cluster track $\vec{X}_c$ for: (black) observations, (red) COAWST model, and (green) NearCom model. Initial cluster track positions are shown by open circles and the location separating inner and outer inlets is indicated by large magenta dots. Bathymetry is colored (scale on the right).

alongshore propagating tides producing asymmetric flows in the inlet region [*van der Vegt et al.*, 2009].

To test the sensitivity of modeled drifter paths on the drifter release location, a numerical experiment was performed in which modeled drifters were released close to (every 10 m within a 50 × 50 m square), but not at the observed drifter release locations. For this experiment, modeled drifter tracks were not significantly different than the model tracks reported, namely, modeled drifters still preferentially exited the new channel and in general had smaller alongshore displacements than the observed drifters. Hence, modeled drifter tracks are not sensitive to the precise release location as long as it is close to the observed release location.

Model drifter cluster velocities ($\vec{U}_c(t)$) and spreading rates (μ) are calculated in the same manner as the observations (see section 5.2). Clusters are based upon drifters exiting either the old or new channels (and not drifter initial locations), thus the observed, COAWST, and NearCom clusters are determined independently of each other and do not necessarily include the same drifters. Consequently, the number of drifters in observed and modeled clusters differ in addition to observed and modeled clusters having different initial positions. The observed and modeled d2r1-old drifter cluster is compared in detail as this is the only case where observed, COAWST, and NearCom modeled clusters all exit the old channel (Figure 12). Moreover, for this case, all three clusters turn left toward $+y$ near the transition from inner to outer inlet, although the observed cluster turns more sharply left than modeled clusters (Figure 12).

Comparing the observed with the modeled downstream l dependence of $|U_c|$ indicates that the observed d2r1-old cluster velocity $|\vec{U}_c|$ is consistently larger than modeled and the observed and modeled l dependence differs (compare black curves Figures 13a–13c). In particular, observed $|\vec{U}_c| \geq 0.6\,\mathrm{m\,s^{-1}}$ for $l < 300$ m while COAWST and NearCom $|\vec{U}_c| \geq 0.6\,\mathrm{m\,s^{-1}}$ only for $l < -700$ m. From the release point ($l = -1400$ m), the observed cluster initially accelerates from 0.7 to 1.0 $\mathrm{m\,s^{-1}}$ near $l = -550$ m, and subsequently decelerates roughly linearly with l. In contrast, COAWST and NearCom models do not reproduce the observed cluster acceleration for $l < -550$ m, and both models have near-release maximum $|\vec{U}_c| \approx 0.8\,\mathrm{m\,s^{-1}}$, and a decreasing $|\vec{U}_c|$ trend toward the outer inlet. These cluster velocities are consistent with the larger observed than modeled ADCP ebb velocities in the old channel (Figure 4c, the ADCP location corresponds to $l \approx -500$ m). The observed slope $d|\vec{U}_c|/dl$ in the linear decelerating region is 50% larger than modeled (gray dashed lines in Figure 13).

Some features of the observed cluster spreading rate μ are modeled well, and others are not. For the d1r1 release, upon exiting the inlet (near $(x, y) \approx (800, 200)$ m in Figure 11) both COAWST and NearCom modeled drifter trajectories spread much less than observed. This is evident also in the d2r1-old spreading rate dependence on downstream distance l (Figure 13). Near the release location ($l < -700$ m), observed, COAWST, and NearCom μ are relatively small (Figure 13, red curves). Unlike the model clusters, observed clusters are squeezed into the old channel ($l \approx -300$ m) resulting in large negative spreading rates ($\mu \approx -5\,\mathrm{m^2\,s^{-1}}$). Also, the observed clusters expand ($\mu > 0$) farther downstream, whereas the modeled spreading rates are near zero.

The observed and modeled features of all 11 clusters (Figure 14) are consistent with the d1r1 release (Figure 11) and d2r1-old clusters (Figure 13). Observed clusters are more likely to exit the old channel (6

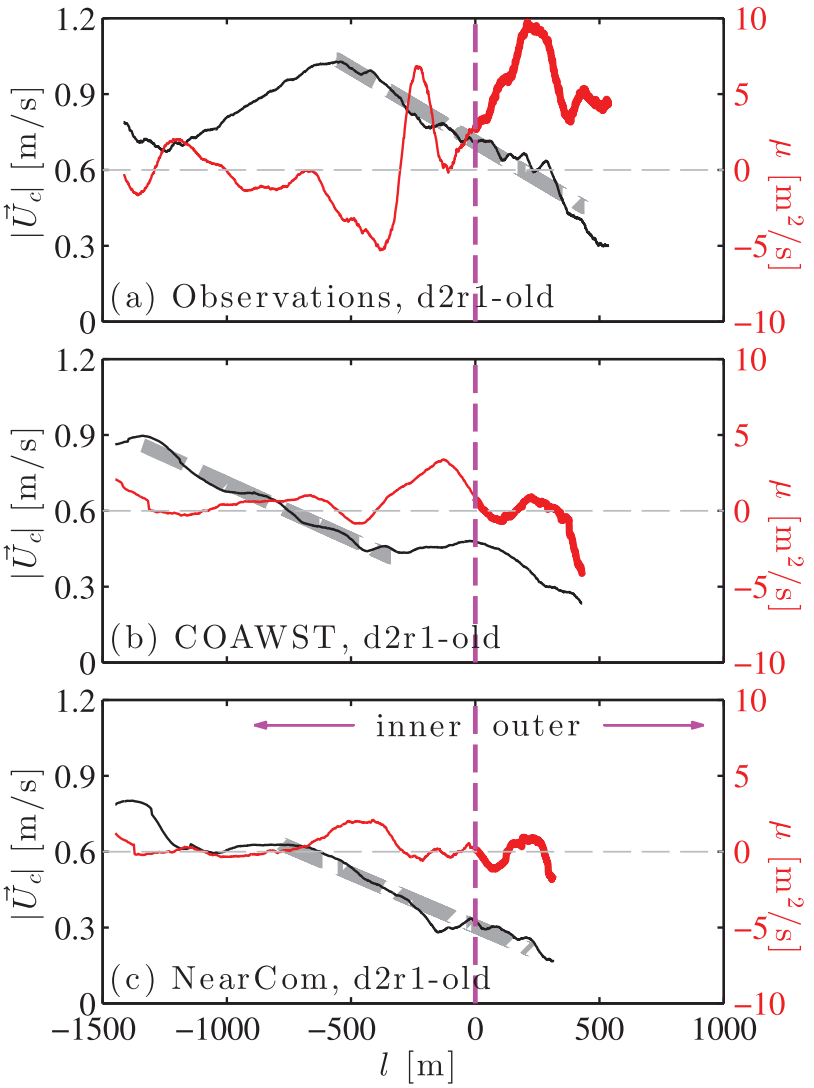

Figure 13. The d2r1-old cluster velocity magnitude $|\vec{U}_c|$ (black) and spreading rate μ (red) versus downstream distance l for: (a) observations, (b) COAWST, and (c) NearCom. The point separating the inner and outer inlet is $l = 0$. The decelerating $|U_c|$-l best fit lines are indicated by thick dashed gray lines. Spreading rates for $l < 0$ are thin red curves (i.e., μ_{in}) and for $l > 0$ are thick red curves (i.e., μ_{out}).

of 11 clusters) relative to the COAWST (2 of 11) and NearCom (3 of 11) clusters. Observed cluster exit paths are more varied and spread across the inlet than modeled clusters (Figure 14). After exiting, observed and COAWST clusters turn left (toward $+y$) more strongly than NearCom clusters. Consistent with the shorter modeled than observed cluster tracks (Figures 13 and 14), COAWST and NearCom cluster velocities are 87% and 66%, respectively, of the observations when averaged along track and over all 11 clusters. Shorter cluster tracks and smaller cluster velocities reflect the weaker modeled than observed Eulerian velocities in the old channel and at the seaward edge of the ebb shoal (locations B and C in Figures 4c and 4e). Differences between observed and modeled cluster trajectories are not improved significantly by including drifter windage effects [*Schmidt et al.*, 2003] equal to 1% of the wind speed in the models.

Overall, observed and modeled spreading rates are smaller in the inner inlet than in the outer inlet (fewer warm colors shoreward of magenta dots in Figure 14, especially in the more populated new channel). The averaged inner-inlet spreading rates μ_{in} for observed and model (COAWST and NearCom) clusters are small $\mu_{in} \leq 0.5\,m^2\,s^{-1}$. In contrast, the outer-inlet observed average $\mu_{out} = 2.8\,m^2\,s^{-1}$ is much larger than modeled $\mu_{out} \approx 0.7\,m^2\,s^{-1}$ (Figure 14). Due to different observed and modeled trajectory lengths, observed and modeled mean outer inlet spreading rates are calculated over different regions. However, an experiment was performed in

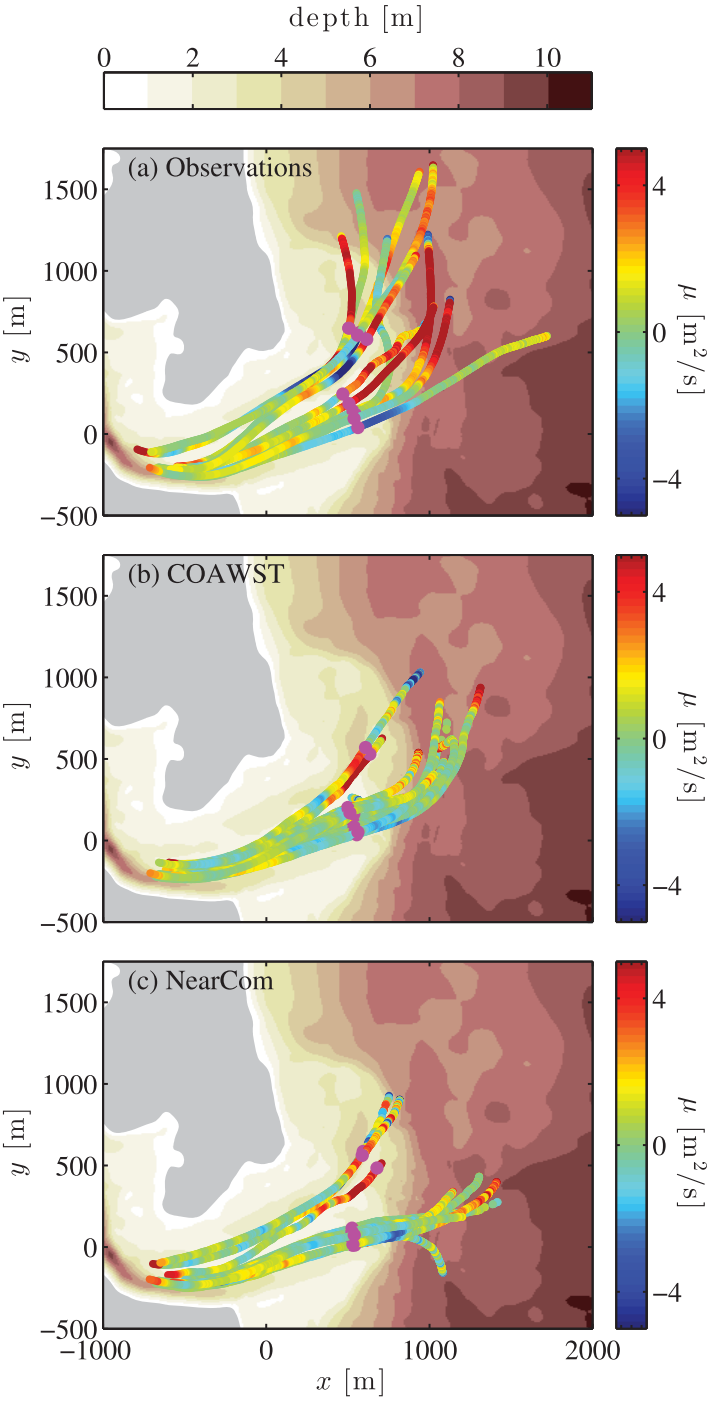

Figure 14. Cluster spreading rates μ colored (scale on right) on the cluster track $\vec{X}_c$ for (a) observations, (b) COAWST, and (c) NearCom. All 11 clusters are shown with only the first 2 h of d3r1 included. Magenta dots separate inner and outer spreading regions. Bathymetry is colored (scale at the top).

which modeled drifters were allowed to propagate farther onto the shelf by advecting modeled drifters for 2 h longer than the observed. For this experiment, the results are not different than those reported and modeled outer inlet spreading rates are still small relative to the observed.

7. Discussion: Spreading and Stratification

The observed and modeled cluster spreading rates μ are different in the outer inlet and deeper coastal ocean (Figure 14). The causes of this difference are investigated by examining the relationship between μ, $\vec{U}_c$, and water depth h. For 2-D-horizontal flow (i.e., shallow water equations), an initial material volume of incompressible fluid is conserved, but laterally expands or contracts as the water depth varies [e.g., *Vallis*, 2006]. A cylindrical material volume $V_0 = Ah$ with area $A = \pi D$ and depth h, whose material derivative $dV_0/dt = 0$, requires $(dA/dt)h + A(dh/dt) = 0$. Substituting $\mu = (1/2\pi)(dA/dt)$, $A(t) = V_0/h(t)$, and $dh/dt = \vec{U}_c(t) \cdot \nabla h$, into this expression yields,

$$\mu = -\frac{V_0}{2\pi}(\vec{U}_c \cdot \nabla h)h^{-2}. \quad (6)$$

Thus, a negative μ is expected for a cluster entering deeper water (positive $(\vec{U}_c \cdot \nabla h)$). For all 11 ebb clusters, and for the outer-inlet spreading rates, the modeled binned-mean μ_{out} and $(\vec{U}_c \cdot \nabla h)h^{-2}$ are linearly related with the negative slope expected for a 2-D-horizontal flow (red and green in Figure 15). Thus, model drifter spreading rates are due to the 2-D hydrodynamics of the models. In contrast, the slope between observed binned-mean μ_{out} and $(\vec{U}_c \cdot \nabla h)h^{-2}$ is positive (black in Figure 15), which is inconsistent with 2-D flow hydrodynamics. These observed and modeled differences are not likely due to model bathymetry resolution or ocean boundary conditions because modeled and observed hydrodynamics are different.

Modeled and observed outer inlet spreading are fundamentally different, likely due to the evolution of the buoyant plume carrying the drifters [*Liu et al.*, 2008]. Although currents in the inlet channels and on the ebb

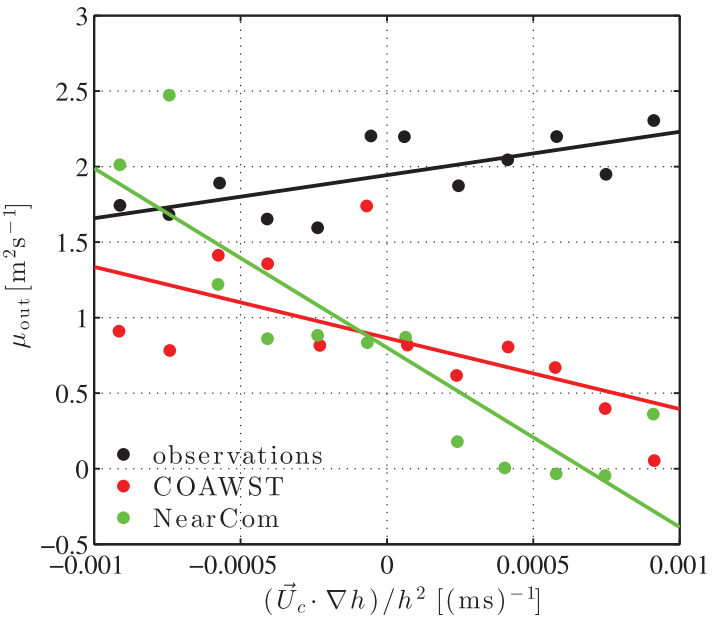

Figure 15. Observed (black), COAWST (red), and NearCom (green) binned mean outer inlet spreading rates (μ_{out}) versus $(\vec{U}_c \cdot \nabla h)h^{-2}$. Solid lines are best fits to the binned means.

shoals are approximately vertically uniform owing to strong currents and the relatively shallow depths (Figure 6), stratification offshore of the inlet mouth was observed during the experiment. In particular, after 16 May and farther offshore, a slightly warm and fresh plume, with both old and new channel contributions, was observed more than 2 km offshore using an AUV [*Rogowski et al.*, 2014]. Additionally, vertical profiles of salinity and temperature on 1 May (Figure 16) in 8 m water depth offshore of the new channel (near $(x, y) \approx (970, 0)$ m, yellow in Figure 1) indicate that stratification was present during ebb drifter releases, although the inlet-ocean density difference is small ($\Delta\rho = 1$ kg m^{-3}, Figure 16c). The 1 May vertical profiles show a thin, fresh ($S = 35.3$ psu), warm ($T = 21.4\,^{\circ}$C) layer of inlet water above salty and colder ($S = 35.8$ psu and $T = 20\,^{\circ}$C) ocean water (see white dashed curves Figures 16a and 16b). Solar heating slightly warms, and weak freshwater inflow slightly freshens, the shallow New River Inlet estuary water.

For buoyant plumes, as the surface water slows, spreads, and thins, it also entrains deeper water cooling the upper layer [e.g., *Yuan and Horner-Devine*, 2013]. For the ebb-tide Columbia River plume, the entrainment of saltier water into the fresher plume water was observed using CTD equipped drifters [*McCabe et al.*, 2008]. For the d1r1 release, cluster temperatures decreased as drifter clusters exited the old-channel, decelerated, and spread (Figure 10). Within the inner-inlet ($l < 0$ m), the cluster temperature initially increases, likely due to solar heating, reaching a maximum near the inner-to-outer inlet boundary (see green curves in Figure 10). For $l > 0$, the drifter cluster decelerates rapidly (gray dashed in Figure 10), and the cluster spreading rate μ increases (red in Figure 10), and the cluster temperature concurrently drops by $\Delta T = 0.25\,^{\circ}$C (green in Figure 10b). This is qualitatively consistent with a two-layer buoyant plume and deeper-water entrainment [*Yuan and Horner-Devine*, 2013]. Decreasing drifter cluster temperature for $l > 0$ was observed for 8 of the 11 clusters, further suggesting that the observed non-2-D drifter spreading (Figure 15) is likely due to buoyant plume effects.

Entrainment rates can be estimated from cluster velocity magnitude $|\vec{U}_c|$ and temperature T_c using the same arguments from which entrainment rates for the Columbia River plume were estimated using drifter velocities and salinities [*McCabe et al.*, 2008]. With modification for temperature entrainment, the vertical entrainment velocity for a steady plume is

$$w_E = \frac{h_{pl}|\vec{U}_c|}{\Delta T}\frac{dT_c}{dl}, \tag{7}$$

where h_{pl} is the plume thickness and ΔT is the temperature difference between plume and shelf water. Although the plume is not steady and precise values of these quantities are not available, reasonable estimates can be made. Using the depth that spreading begins for the plume thickness, $h_{pl} \approx 2$ m (Figure 16b), $|\vec{U}_c| \approx 0.5$ m s^{-1} (Figure 10b), $\Delta T \approx 1\,^{\circ}$C (from Figure 16b), and $dT/dl \approx 0.25/1000\,^{\circ}$C m^{-1} (from Figure 10b), results in a cluster entrainment rate $w_e \approx 2.5 \times 10^{-4}$ m s^{-1}, smaller than, but the same order of magnitude estimated for the Columbia River plume [*McCabe et al.*, 2008]. Thus, entrainment rates for weakly stratified systems such as NRI may be comparable to those at larger systems such as the Columbia River.

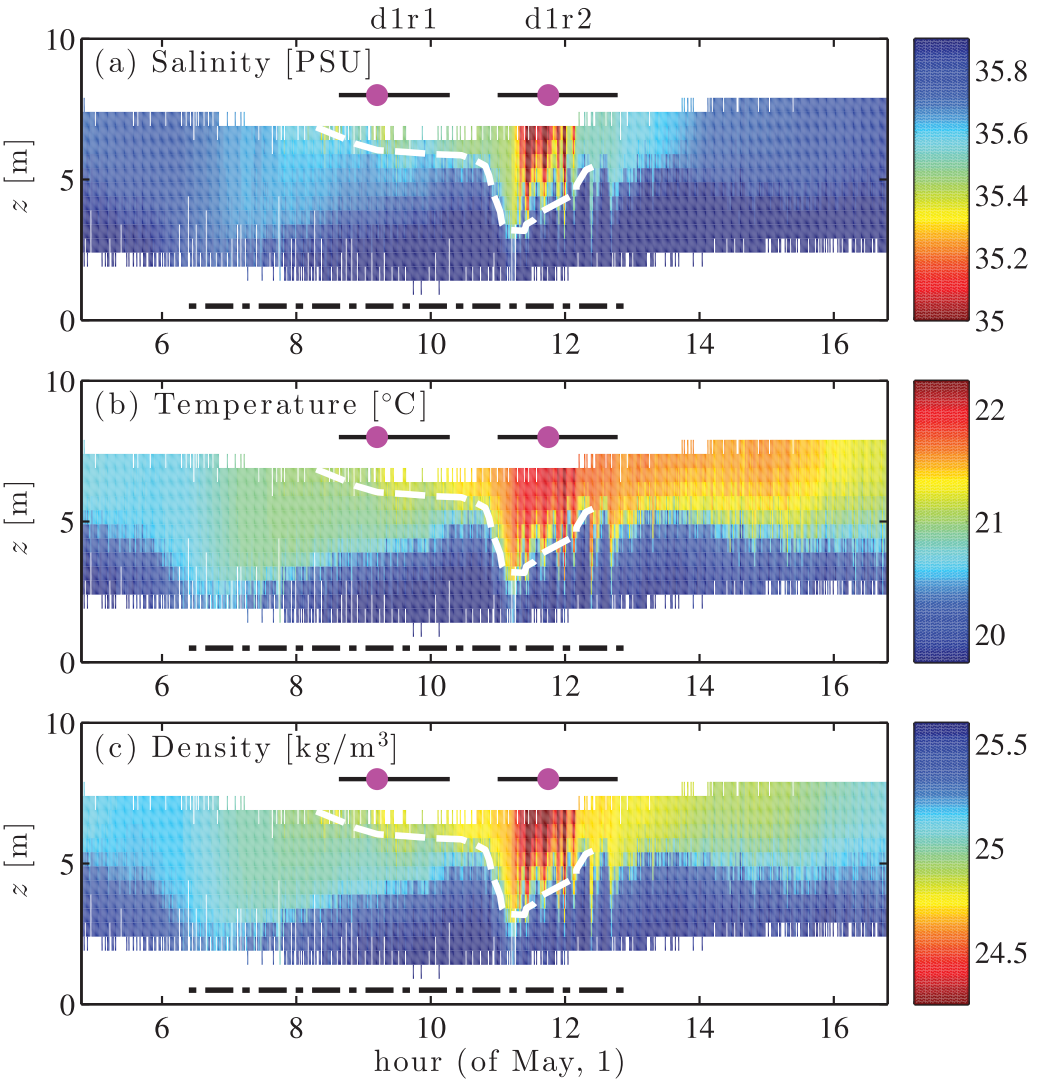

Figure 16. (a) Salinity, (b) temperature, and (c) density (σ) versus height above the bed z and time from the wirewalker at $(x, y) = (1000, 0)$ m in roughly 8 m water depth (yellow marker in Figure 1). The white dashed curve represents the water mass boundary of new warm and fresh inlet water. The horizontal black dash-dot line at the bottom of each plot represents the duration of ebb tide, i.e., $u > 0$. The solid black horizontal lines indicate the duration of the d1r1 and d1r2 releases. Magenta dots indicate the approximate time that clusters reached the outer inlet. Color scales are on the right.

8. Summary and Conclusions

Transport and spreading near the mouth of a narrow, shallow, weakly stratified tidal inlet (New River Inlet, NC) are investigated using GPS-tracked drifters and numerical models. For six ebb tide drifter releases, velocities are largest (>1 m s^{-1}) in two deep, $\approx$ 30 m wide navigation channels that bisect the 1–3 m deep ebb shoal. In the channels, surface drifter and subsurface current meter velocities are similar (Figure 6), consistent with strong vertical mixing and the essentially 2-D model hydrodynamics. Drifters were preferentially entrained and retained in these channelized jets, and lateral spreading of drifter clusters within a jet was relatively weak (Figures 8 and 9). Upon exiting the inlet mouth at the seaward edge of the ebb shoal, jet velocities decrease linearly with downstream distance (to <0.2 m s^{-1}, about 1 km from shore), a deceleration rate 5 times larger than reported for the Columbia River Mouth [*McCabe et al.*, 2008]. Average spreading rates increase from $\mu_{in} \approx 0.5$ m^2 s^{-1} to $\mu_{out} \approx 3$ m^2 s^{-1} (Figures 10 and 13).

The numerical models COAWST and NearCom do not reproduce the observations quantitatively. For example, observed drifter velocities were larger than modeled (Figure 13), and modeled and observed paths differed in two ways: (1) few modeled (both COAWST and NearCom) drifters exited the old channel, and (2)

modeled (especially NearCom) drifters do not turn left (toward $+y$) as sharply as observed upon exiting the inlet (Figure 11). Observed and modeled Lagrangian velocity differences are consistent with larger observed Eulerian velocities in the old channel (Figure 4c), and more observed drifters exit the old channel due to weaker modeled than observed cross-channel flow in the inlet mouth (Figure 4b). These differences may be due to model tidal boundary conditions, imperfect bathymetry, model resolution, and the assumption of spatially homogeneous winds. Better COAWST than NearCom drifter paths upon exiting the inlet may be due to tidal boundary conditions, suggesting that including progressive tides on the model lateral boundary (as done in COAWST, but not in NearCom) is important.

The model simulations do reproduce qualitatively the relatively small spreading μ in the inner inlet, and the roughly linear jet flow deceleration. However, model spreading in the outer inlet ($\mu_{out} \approx 0.7\,m^2\,s^{-1}$) is much less than observed ($\mu_{out} \approx 2.8\,m^2\,s^{-1}$), and may be due to neglecting stratification in the models. AUV observations [*Rogowski et al.*, 2014] and the profiling wirewalker (Figure 16), show that slightly less dense inlet water often forms a buoyant plume above slightly cooler and saltier ocean water ($\Delta\rho = 1\,kg\,m^{-3}$). Consistent with buoyant plume dynamics, observed drifter temperatures decrease as they spread (Figure 10) indicating the entrainment of deeper water into the surface.

Although stratification effects are understood to be important for systems with large density differences, such as the Columbia River plume with $\Delta\rho \approx 13\,kg\,m^{-3}$ [*McCabe et al.*, 2008], the results presented here suggest that buoyancy effects should be considered in the transition from the outer inlet to the coastal ocean even for weakly stratified systems. Thus, despite good Eulerian velocity model-data comparison at many locations within the inlet and the coastal ocean using unstratified models such as NearCom and COAWST [*Chen et al.*, 2015; Olabarrieta et al., manuscript in preparation, 2015], simulating Lagrangian transport and fate through a tidal inlet onto the coastal ocean likely requires using stratified models.

Acknowledgments
Supported by NSF, ONR, and ASD (R+E). Staff and students from the Integrative Oceanography Division (B. Woodward, B. Boyd, K. Smith, D. Darnell, K. Hally-Rosendahl, R. Grenzeback, and A. Doria) and WHOI (L. Gorrell, D. Forsman, S. Kilgallin, C. Rivera-Erick, R. Yopak, S. Zippel, D. Clark, A. Wargula, M. Moulton, and M. Orescanin) were instrumental in the data collection. Support to J. L. Chen is provided by ONR (N00014-13-1-0120) to the University of Delaware. Data used in this article can be obtained from Matthew Spydell (mspydell@ucsd.edu) or Falk Feddersen (falk@coast.ucsd.edu) in accordance with AGU data policies. We thank two anonymous reviewers for helping to improve the manuscript. Also, N. Kumar and S. H. Suanda are thanked as they provided helpful feedback.

References

Arega, F., S. Armstrong, and A. W. Badr (2008), Modeling of residence time in the East Scott Creek Estuary, South Carolina, USA, *J. Hydroenviron. Res.*, *2*, 99–108, doi:10.1016/j.jher.2008.07.003.

Berloff, P., and J. McWilliams (2002), Material transport in oceanic gyres. Part II: Hierarchy of stochastic models, *J. Phys. Oceanogr.*, *32*(3), 797–830.

Bertin, X., A. B. Fortunato, and A. Oliveira (2009), A modeling-based analysis of processes driving wave-dominated inlets, *Cont. Shelf Res.*, *29*(5–6), 819–834, doi:10.1016/j.csr.2008.12.019.

Bilgili, A., J. A. Proehl, D. R. Lynch, K. W. Smith, and M. R. Swift (2005), Estuary/ocean exchange and tidal mixing in a Gulf of Maine Estuary: A Lagrangian modelling study, *Estuarine Coastal Shelf Sci.*, *65*, 607–624, doi:10.1016/j.ecss.2005.06.027.

Booij, N., R. C. Ris, and L. H. Holthuijsen (1999), A third-generation wave model for coastal regions: 1. Model description and validation, *J. Geophys. Res.*, *104*(C4), 7647–7666, doi:10.1029/98JC02622.

Bruun, P. (1978), *Stability of Tidal Inlets: Theory and Engineering*, 510 pp., Elsevier Sci., Amsterdam.

Chassignet, E. P., H. G. Arango, D. Dietrich, T. Ezer, M. Ghil, D. B. Haidvogel, C. C. Ma, A. Mehra, A. M. Paiva, and Z. Sirkes (2000), DAMEE-NAB: The base experiments, *Dyn. Atmos. Oceans*, *32*, 155–183, doi:10.1016/S0377-0265(00)00046-4.

Chen, C., J. Qi, C. Li, R. C. Beardsley, H. Lin, R. Walker, and K. Gates (2008), Complexity of the flooding/drying process in an estuarine tidal-creek salt-marsh system: An application of FVCOM, *J. Geophys. Res.*, *113*, C07052, doi:10.1029/2007JC004328.

Chen, F., D. G. MacDonald, and R. D. Hetland (2009), Lateral spreading of a near-field river plume: Observations and numerical simulations, *J. Geophys. Res.*, *114*, C07013, doi:10.1029/2008JC004893.

Chen, J. L., F. Hsu, T. J. Shi, B. Raubenheimer, and S. Elgar (2015), Hydrodynamic and sediment transport modeling of New River Inlet (NC) under the interaction of tides and waves, *J. Geophys. Res. Oceans*, *120*, doi:10.1002/2014JC010425.

de Brauwere, A., B. de Brye, S. Blaise, and E. Deleersnijder (2011), Residence time, exposure time and connectivity in the Scheldt Estuary, *J. Mar. Syst.*, *84*, 85–95, doi:10.1016/j.jmarsys.2010.10.001.

Dodet, G., X. Bertin, N. Bruneau, A. B. Fortunato, A. Nahon, and A. Roland (2013), Wave-current interactions in a wave-dominated tidal inlet, *J. Geophys. Res. Oceans*, *118*, 1587–1605, doi:10.1002/jgrc.20146.

Garvine, R. W. (1999), Penetration of buoyant coastal discharge onto the continental shelf: A numerical model experiment, *J. Phys. Oceanogr.*, *29*, 1892–1909, doi:10.1175/1520-0485(1999)029<1892:POBCDO >2.0.CO;2.

Geyer, W. R. (1997), Influence of wind on dynamics and flushing of shallow estuaries, *Estuarine Coastal Shelf Sci.*, *44*, 713–722, doi:10.1006/ecss.1996.0140.

Haas, K. A., and J. C. Warner (2009), Comparing a quasi-3D to a full 3D nearshore circulation model: SHORECIRC and ROMS, *Ocean Modell.*, *26*, 91–103, doi:10.1016/j.ocemod.2008.09.003.

Haidvogel, D. B., H. G. Arango, K. Hedstrom, A. Beckmann, P. Malanotte-Rizzoli, and A. F. Shchepetkin (2000), Model evaluation experiments in the North Atlantic Basin: Simulations in nonlinear terrain-following coordinates, *Dyn. Atmos. Oceans*, *32*, 239–281, doi:10.1016/S0377-0265(00)00049-X.

Haidvogel, D. B., et al. (2008), Regional ocean forecasting in terrain-following coordinates: Model formulation and skill assessment, *J. Comput. Phys.*, *227*(7), 3595–3624, doi:10.1016/j.jcp.2007.06.016.

Hench, J. L., and R. A. Luettich (2003), Transient tidal circulation and momentum balances at a shallow inlet, *J. Phys. Oceanogr.*, *33*, 913–932, doi:10.1175/1520-0485(2003)33<913:TTCAMB>2.0.CO;2.

Hetland, R. D., and D. G. MacDonald (2008), Spreading in the near-field Merrimack River plume, *Ocean Modell.*, *21*, 12–21, doi:10.1016/j.ocemod.2007.11.001.

Kumar, N., G. Voulgaris, J. Warner, and M. Olabarrieta (2012), Implementation of the vortex force formalism in the coupled ocean-atmosphere-wave-sediment transport (COAWST) modeling system for inner shelf and surf zone applications, *Ocean Modell.*, *47*, 65–95, doi:10.1016/j.ocemod.2012.01.003.

Kumar, N., F. Feddersen, Y. Uchiyama, J. McWilliams, and W. O'Reilly (2015), Mid-shelf to surf zone coupled ROMS-SWAN model-data comparison of waves, currents, and temperature: Diagnosis of subtidal forcings and response, *J. Phys. Oceanogr.*, *45*, 1464–1490, doi: 10.1175/JPO-D-14–0151.1.

Liu, W., W. Chen, J. Kuo, and C. Wu (2008), Numerical determination of residence time and age in a partially mixed estuary using three-dimensional hydrodynamic model, *Cont. Shelf Res.*, *28*, 1068–1088, doi:10.1016/j.csr.2008.02.006.

Malhadas, M. S., P. C. Leitão, A. Silva, and R. Neves (2009), Effect of coastal waves on sea level in Óbidos Lagoon, Portugal, *Cont. Shelf Res.*, *29*(9), 1240–1250, doi:10.1016/j.csr.2009.02.007.

Malhadas, M. S., R. J. Neves, P. C. Leitão, and A. Silva (2010), Influence of tide and waves on water renewal in Óbidos Lagoon, Portugal, *Ocean Dyn.*, *60*, 41–55, doi:10.1007/s10236-009-0240-3.

McCabe, R. M., B. M. Hickey, and P. MacCready (2008), Observational estimates of entrainment and vertical salt flux in the interior of a spreading river plume, *J. Geophys. Res.*, *113*, C08027, doi:10.1029/2007JC004361.

McCabe, R. M., P. MacCready, and B. M. Hickey (2009), Ebb-tide dynamics and spreading of a large river plume*, *J. Phys. Oceanogr.*, *39*, 2839–2856, doi:10.1175/2009JPO4061.1.

McWilliams, J. C., J. M. Restrepo, and E. M. Lane (2004), An asymptotic theory for interaction of waves and currents in coastal waters, *J. Fluid Mech.*, *511*, 135–178, doi:10.1017/S0022112004009358.

Olabarrieta, M., J. C. Warner, and N. Kumar (2011), Wave-current interaction in Willapa Bay, *J. Geophys. Res.*, *116*, C12014, doi:10.1029/2011JC007387.

Olabarrieta, M., R. Geyer, and N. Kumar (2014), The role of morphology and wave-current interaction at tidal inlets: An idealized modeling analysis, *J. Geophys. Res. Oceans*, *119*, 8818–8837, doi:10.1002/2014JC010191.

Orescanin, M., B. Raubenheimer, and S. Elgar (2014), Observations of wave effects on inlet circulation, *Cont. Shelf Res.*, *82*, 37–42, doi: 10.1016/j.csr.2014.04.010.

Putrevu, U., and I. A. Svendsen (1999), Three-dimensional dispersion of momentum in wave induced nearshore currents, *Eur. J. Mech. B*, *18*, 409–427.

Rogowski, P., E. Terrill, and J. L. Chen (2014), Observations of the frontal region of a buoyant river plume using an autonomous underwater vehicle, *J. Geophys. Res. Oceans*, *119*, 7549–7567, doi:10.1002/2014JC010392.

Schmidt, W. E., B. T. Woodward, K. S. Millikan, R. T. Guza, B. Raubenheimer, and S. Elgar (2003), A GPS-Tracked surf zone drifter, *J. Atmos. Oceanic Technol.*, *20*(7), 1069–1075.

Shchepetkin, A. F., and J. C. McWilliams (2005), The regional oceanic modeling system (ROMS): A split-explicit, free-surface, topography-following-coordinate oceanic model, *Ocean Modell.*, *9*(4), 347–404, doi:10.1016/j.ocemod.2004.08.002.

Shi, F., I. A. Svendsen, J. T. Kirby, and J. M. Smith (2003), A curvilinear version of a Quasi-3D nearshore circulation model, *Coastal Eng.*, *49*, 99–124, doi:10.1016/S0378-3839(03)00049-8.

Svendsen, I. A., K. Haas, and Q. Zhao (2004), *Quasi-3D Nearshore Circulation Model SHORECIRC: Version 2.0*, 64 pp., Univ. of Del., Newark.

Uchiyama, Y., J. C. McWilliams, and A. F. Shchepetkin (2010), Wave-current interaction in an oceanic circulation model with a vortex force formalism: Application to the surf zone, *Ocean Modell.*, *34*, 16–35, doi:10.1016/j.ocemod.2010.04.002.

Vallis, G. K. (2006), *Atmospheric and Oceanic Fluid Dynamics*, 745 pp., Cambridge Univ. Press, Cambridge, U. K.

van der Vegt, M., H. M. Schuttelaars, and H. E. de Swart (2009), The influence of tidal currents on the asymmetry of tide-dominated ebb-tidal delta, *Cont. Shelf Res.*, *29*, 159–174, doi:10.1016/j.csr.2008.01.018.

Wargula, A., B. Raubenheimer, and S. Elgar (2014), Wave-driven along-channel subtidal flows in a well-mixed ocean inlet, *J. Geophys. Res. Oceans*, *119*, 2987–3001, doi:10.1002/2014JC009839.

Warner, J. C., B. Armstrong, R. He, and J. B. Zambon (2010), Development of a Coupled Ocean-Atmosphere-Wave-Sediment Transport (COAWST) modeling system, *Ocean Modell.*, *35*, 230–244, doi:10.1016/j.ocemod.2010.07.010.

Xu, D., and H. Xue (2011), A numerical study of horizontal dispersion in a macro tidal basin, *Ocean Dyn.*, *61*, 623–637, doi:10.1007/s10236-010-0371-6.

Yuan, D., B. Lin, and R. A. Falconer (2007), A modelling study of residence time in a macro-tidal estuary, *Estuarine Coastal Shelf Sci.*, *71*, 401–411, doi:10.1016/j.ecss.2006.08.023.

Yuan, Y., and A. R. Horner-Devine (2013), Laboratory investigation of the impact of lateral spreading on bouyancy flux in a river plume, *J. Phys. Oceanogr.*, *43*, 2588–2610, doi:10.1175/JPO-D-12-0117.1.